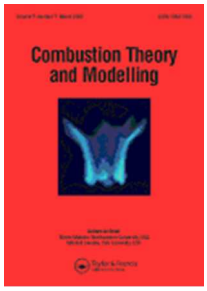

Computational study of lean premixed turbulent flames using RANS-PDF and LES-PDF methods

Journal:	*Combustion Theory and Modelling*
Manuscript ID:	Draft
Manuscript Type:	Original Manuscript
Date Submitted by the Author:	n/a
Complete List of Authors:	Rowinski, David; Cornell University, Sibley School of Mechanical and Aerospace Engineering Pope, Stephen; Cornell University, Sibley School of Mechanical and Aerospace Engineering
Keywords:	turbulent combustion, lean premixed flames, molecular diffusion, detailed chemistry, PDF methods

Combustion Theory and Modelling
Vol. 00, No. 00, November 2012, 1–22

RESEARCH ARTICLE

Computational study of lean premixed turbulent flames using RANS-PDF and LES-PDF methods

David H. Rowinski[a]* and Stephen B. Pope[a]

[a]*Sibley School of Mechanical and Aerospace Engineering, Cornell University, Ithaca, NY, 14853, USA*

(*November 2012*)

A computational study is performed on a series of four piloted, lean, premixed turbulent jet flames. These flames use the Sydney Piloted Premixed Jet Burner (PPJB), and with jet velocities of 50, 100, 150, and 200 m/s are denoted PM1-50, PM1-100, PM1-150, and PM1-200 respectively. Calculations are performed using RANS-PDF and LES-PDF methodologies, with different treatments of molecular diffusion, with detailed chemistry and flamelet-based chemistry modeling, and using different imposed boundary conditions. The sensitivities of the calculations to these different aspects of the modeling are compared and discussed. Comparisons are made to experimental data and to previously-performed calculations. It is found that, given suitable boundary conditions and treatment of molecular diffusion, excellent agreement between the calculations and experimental measurements of the mean and variance fields can be achieved for PM1-50 and PM1-100. The application of a recently developed implementation of molecular diffusion results in a large improvement in the computed variance fields in the LES-PDF calculations. The inclusion of differential diffusion in the LES-PDF calculations provides insight on the behavior in the near-field region of the jet, but its effects are found to be confined to this region and to the species CO, OH, and H_2. A major discrepancy observed in many previous calculations of these flames is an overprediction of reaction progress in PM1-150 and PM1-200, and this discrepancy is also observed in the LES-PDF calculations; however, a parametric study of the LES-PDF mixing model reveals that, with a sufficiently large mixing frequency, calculations of these two flames are capable of yielding improved reaction progress in good qualitative agreement with the mean and RMS scalar measurements up to x/D of 30. Lastly, the merits of each computational methodology are discussed in light of their computational costs.

Keywords: turbulent combustion; lean premixed flames; molecular diffusion; detailed chemistry; PDF methods

1. Introduction

1.1 Motivation for a Computational Study of Lean Premixed Combustion

Turbulent combustion is currently responsible for generating around 80% of the world's energy supply [1]. Given the world's growing needs for energy and, at the same time, reduced emissions of pollutants, understanding turbulent combustion is of prime practical importance. A better understanding of this intricate physical process, and the ability to incorporate this understanding into computational models, will ultimately lead to the ability to design combustion devices that can produce energy more efficiently, more reliably, and more cleanly.

*Corresponding author. Email: dhr46@cornell.edu

ISSN: 1364-7830 print/ISSN 1741-3559 online

DOI: 10.1080/13647830.YYYY.xxxxxx
http://www.tandfonline.com

One particular mode of combustion that yields improved efficiency and reduced emissions is lean premixed combustion [2–4]. With a lean pre-mixture of fuel and oxidizer, the flame temperature is substantially reduced, resulting in decreased production of pollutants such as NO_x. Since the reacting mixture is fuel-lean, the abundance of oxidizer ensures a more complete burning of the fuel; the amount of products of incomplete combustion, such as CO and unburned hydrocarbons, is reduced.

However, lean combustion is subject to instabilities [5–7]. These instabilities take the form of complex turbulence-chemistry interactions such as local extinction of the flame. They occur when the turbulence intensity is high, and the fuel is near its flammability limit. To ensure that combustion devices can be designed for safe and reliable operation while utilizing lean premixed combustion, it is essential to ensure that the computational models are able to capture these phenomena. Therefore, a set of experiments has been developed [10, 10, 10] in which these turbulent-chemistry interactions are present to various degrees, and detailed measurements have been made to allow comparison to model predictions.

1.2 Description of the Experiments to be Studied

The Sydney Piloted Premixed Jet Burner (PPJB) was developed to test turbulence-chemistry interactions at lean and highly turbulent conditions [10, 10, 10]. The burner consists of three main streams: a jet, a pilot, and a coflow. The central jet is lean, premixed methane-air exiting at a high velocity. Surrounding the jet is a hot pilot of stoichiometric methane-air combustion products at a low velocity. Around the pilot is a hot coflow of lean hydrogen-air products. More detailed information on the bulk properties of the inflowing streams is presented in Table 1. The diameter of the central jet, D, is 4 mm, and is taken to be a reference length scale throughout this study.

Four different flames are studied on the PPJB, and differ only in the bulk velocity of the central jet. The four flames are denoted as PM1-50, PM1-100, PM1-150, and PM1-200 with jet bulk velocities of 50, 100, 150, and 200 m/s, respectively. The Reynolds number, Re, based on the bulk velocity of the jet, the jet diameter, and the unburned jet composition, increases from 12,500 in PM1-50 to 50,000 in PM1-200. As the jet bulk velocity increases, the luminosity of each flame is observed to vary differently in the axial direction. Flames PM1-50 and PM1-100 have strong luminosity throughout the length of the flame. Flame PM1-150 exhibits reduced luminosity between x/D of 15 and x/D of 45. Flame PM1-200 has the most drastic reduction in luminosity, extending from x/D of 7.5 to x/D of 45. Beyond x/D of 45 there is a very faint increase in the flame luminosity, suggesting that burning begins to increase in intensity around this region.

Detailed measurements of both velocity and scalar statistics have been made for these four flames. The burner is characterized and the stability of the flames is explored as a function of the jet equivalence ratio and bulk velocity in [10]. By seeding the jet with particles, laser doppler velocimetry is used to measure the mean and fluctuating axial and radial components of velocity [10]. Simultaneous two-dimensional images of both temperature and the mass fraction of OH are obtained using Rayleigh-OH planar laser-induced fluorescence (PLIF) [10]. The thermochemical composition throughout these flames is further revealed through simultaneous line measurements of temperature and mass fractions of the chemical species CH_4, O_2, N_2, H_2, H_2O, CO_2, CO, and OH, from which radial profiles of the mean and RMS of these quantities are obtained [10]. These measurements are made using the Raman-Rayleigh procedure. Additionally, measurements of the CO

mass fraction are made using laser-induced fluorescence (LIF) and measurements of the OH mass fraction are made using PLIF. Lastly, simultaneous imaging of temperature and the mass fractions of OH and CH_2O is performed to further explore the finite-rate chemistry effects in these flames [10].

1.3 Previous Calculations of this Flame Series

Several previous studies of this flame have been performed or are currently in progress. In [10], a hybrid Reynolds-Averaged Navier Stokes (RANS) and transported composition probability density function (PDF) method is used to make calculations of all four flames. The calculations use two-equation turbulence models and detailed chemistry. It is found that the flame length is underpredicted in the calculations, as a result of both the jet spreading too rapidly, and the reaction progress being overpredicted. A study of the mixing model constant, C_ϕ, shows that larger values of C_ϕ result in a cross product of CO and OH mole fractions, $CO \times OH$, with qualitative behavior in better agreement with the experimental measurements. However, the magnitude of $CO \times OH$ is over an order of magnitude too large in these calculations, and the scalar statistics such as the RMS temperature do not agree quantitatively with the measurements, so the effect of C_ϕ is still ambiguous.

In [11], a hybrid RANS and joint velocity - turbulence frequency - composition PDF method is used to model all the flames in the series. Calculations of the mean and RMS species mass fractions and temperature are in reasonable agreement with the experimental measurements for flame PM1-50. For flame PM1-200, the mean and RMS mixture fractions are in good agreement with the experimental data for all locations at which measurements have been taken; however, the mean temperature is substantially overpredicted and the mean fuel mass fraction is underpredicted, showing that the reaction progress is overpredicted in the calculations. A comprehensive set of sensitivity studies is performed on flame PM1-200 to examine the effect of nearly all aspects of the modeling on the amount of reaction progress calculated for PM1-200. This study involves the use of different detailed chemical mechanisms, mixing models, mixing model constants, turbulence model constants, and inflow boundary conditions. No parameter in the investigated parameter space yields a significant reduction of the reaction progress, and it is reasoned that the mixing models are the largest source of modeling uncertainty. These calculations also suffer from poor predictions of mixture fractions and temperature in the near field of the mixing layer between the pilot and coflow streams. Lastly, the results are sensitive to the value of the turbulence model constant $C_{\omega 1}$, which controls the spreading rate of the jet; a value of 0.70 is used to adequately calculate the spreading rate of the jet, which is the same as the value used in some other calculations of jet flames [12], but is slightly larger than the values of 0.56 and 0.65 used more commonly in previous studies of jet flames [12–14].

In [15], LES calculations of PM1-100 are performed. In these calculations, the filtered reaction source term is taken from the reaction source term evaluated at the filtered composition field, so the effect of subgrid-scale variations in the composition is essentially neglected. The mean velocity field is in good agreement with the experimental measurements. The radial profiles of mean and RMS species mass fractions and temperature are compared at x/D of 2.5, 7.5, and 15. Generally, the agreement between the experimental and calculated mean and RMS scalar fields is good for x/D of 2.5 and 7.5. At x/D of 15, the mean temperature is underpredicted in the pilot region, and overpredicted near the centerline, suggesting that the calculations either overpredict the rate at which the pilot spreads into the

jet or overpredict the reaction progress. The study also finds that 1-step and 2-step chemical mechanisms are insufficient to calculate the mean CO mass fraction and mean temperature accurately using this methodology, whereas a 20-species, 82-reaction skeletal mechanism results in improved predictions of these quantities.

In more recent and ongoing works, [16] uses a RANS and conditional moment closure (CMC) methodology to perform calculations of PM1-50 and PM1-200. The results indicate a behavior of the reaction progress similar to that in [10, 11, 15]; the reduced amount of variables used in the CMC is found to provide description of the chemistry of equal quality to calculations without a reduced-variable description of the flow. In [17], an Eulerian stochastic fields methodology with LES and detailed chemistry is used to make calculations of flame PM1-100. Good agreement in the mean and RMS scalar fields is obtained at x/D of 7.5 and farther downstream at x/D of 45. From x/D of 15 to 30, the mean temperature is overpredicted and the mean fuel mass fraction is underpredicted in the calculations, with observations similar to those in [11, 16]. In [18], a flamelet and progress variable combustion model is used in conjunction with LES. The combustion model uses an additional variable to account for heat loss, which results in improved predictions of the mean temperature. Calculations of PM1-100 show good agreement with the experimental data up to x/D of 15, the last location at which results are presented.

The modeling approaches used in the previous calculations cover a wide range of the currently existing models. However, none of the previous works has proved successful for PM1-150 and PM1-200. Furthermore, most of the calculations of PM1-100 report results only around the near-field of the jet, that is, between x/D of 2.5 and 15, and not further downstream at x/D of 30 or 45.

1.4 Objectives for this Study

In light of the findings of the aforementioned previous works, it is clear that there is much to address regarding the ability of existing models and methodologies to compute the flames PM1-150 and PM1-200 accurately. This work targets four particular components of the modeling: the level of turbulence closure (LES-PDF and RANS-PDF), the description of the chemistry (flamelet-based and detailed chemical kinetics), the treatment of molecular diffusion, and the imposed inflow boundary conditions. The objective of this study is to quantify how sensitive the calculations are to these particular components of the models. The most important model components for accurate calculations of these flames are identified, and the computational cost of each is assessed. This study aims to address all flames in the PPJB series, and to compare results at all relevant locations throughout the flames.

A brief overview of the contents of the remainder of this paper follows. In Sec. 2, the RANS-PDF methodology is described and the computational configuration for those calculations is explained. The implementation of three components of the RANS-PDF model are described and tested, and the effect on the calculations is shown. These three components are: (1) a random walk model for molecular diffusion, (2) a combustion model based on flamelet-generated manifolds (FGM), and (3) inlet boundary conditions. In Sec. 3, the LES-PDF methodology is described along with the computational configuration of the LES-PDF calculations. The numerical accuracy of the LES-PDF calculations is demonstrated, and the effects of molecular diffusion modeling are examined. The focus of the LES-PDF studies is on the effects of differential diffusion and the model constant, C_M. Following the LES-PDF study, the most important results are discussed in Sec. 4 and conclusions are drawn in Sec. 5.

2. RANS-PDF Calculations

One of the notable characteristics of the PPJB flames is the importance of finite-rate chemistry effects. So, when considering modeling these flames, a natural choice for a methodology is a model in which the effects of chemical reaction can be treated exactly. With the probability density function (PDF) method [19–21], this is exactly the case; thus it is the basis of all the computational work performed in this study. A second notable characteristic of the PPJB flames is that these important finite-rate chemistry effects occur in flows of simple geometry. There are no wall effects, swirl, or recirculation, and the flow is statistically axi-symmetric. Therefore, a logical first choice for the type of PDF method used to study these flames is one with turbulence closure based on the Reynolds-Averaged Navier Stokes (RANS) equations. Specifically, the joint velocity-turbulence frequency-composition PDF method [21] is used, in which the joint PDF of the fluctuating velocity, turbulence frequency, and thermochemical composition is solved by a coupled finite-volume solver and particle solver.

RANS-PDF methods have been successfully applied to many jet flames in past studies. The non-premixed methane-air Sandia flames D, E, and F [22] exhibit phenomena of extinction and re-ignition which have been well captured by several RANS-PDF modeling studies [12, 13, 23, 24]. Additionally, the non-premixed lifted hydrogen-air flame in a hot coflow [25] has been the subject of several successful RANS-PDF modeling studies [12, 14, 26, 27]; this flame exhibits a sensitivity to the coflow temperature which has been well-captured by RANS-PDF methods [14]. In addition to non-premixed turbulent jet flames, RANS-PDF methods have also been applied to turbulent premixed jet flames [28–30], including two of the previously mentioned studies of the PPJB [10, 11]. One of the drawbacks of the PDF method is the need to model the effect of molecular diffusion through a mixing model. In several calculations of premixed flames, this aspect of the model has been suggested to be the primary source of modeling error [10, 11, 29], and therefore modeling studies need to be careful to address the sensitivities to the various parameters of these mixing models.

2.1 Joint PDF Computational Methodology

The calculations described in [10, 11] both used RANS-based approaches. The RANS-PDF calculations to be described in this work are based on the same joint velocity-frequency-composition PDF used in [11]. This method is implemented computationally through a coupled finite-volume/particle solver [31].

In the particle solver, Lagrangian particles evolve in position, velocity, turbulence frequency, and composition. The velocity is modeled by the Simplified Langevin Model (SLM) [32]. The turbulence frequency is modeled by a stochastic frequency model [33]. The composition evolves by mixing and chemical reaction. This study uses the EMST mixing model [34], which previous studies [11] have shown to be superior in the PPJB calculations upon comparing scatter plots of the particle composition. The chemical reaction source term is evaluated from detailed chemical kinetics. These calculations use the 16-species ARM-1 mechanism [35], which is shown to yield calculations of these flames of similar quality to those of more detailed mechanisms [11]. The storage-retrieval technique of *in-situ* adaptive tabulation (ISAT) [36, 37] is used to compute the change in composition due to chemical reaction in a computationally efficient manner.

The finite-volume solver solves the mean equations for mass, momentum, energy, and thermochemical state. The particle solver provides the finite-volume solver with

the turbulent fluxes and the mean chemical source term. The finite-volume solver provides the mean density and fluctuating component of velocity to the particle solver. When the solution reaches a statistically stationary state, the statistics are time-averaged until sufficient temporal convergence is attained.

2.2 Numerical Configuration for the RANS-PDF Calculations

The RANS-PDF calculations are preformed on a two-dimensional cylindrical domain as shown in Figure 1. The domain extends $100D$ in the axial direction, where D is the jet diameter and the axial coordinate is denoted by x. The domain extends $40D$ in the radial direction, whose coordinate is denoted by r. The grid size is 144 $\times$ 144 cells in the axial and radial directions. This set up is identical to that used in [11], and the numerical accuracy of such a configuration has previously been assessed. The maximum error in the mean temperature is about 4%, and about 8% for the RMS temperature in PM1-200 [11]. The values for the model constants are shown in Table 2, and are the same used in many previous studies of turbulent jet flames.

Boundary conditions are obtained from separate calculations on an extended domain, ranging from x/D of -100 to 100 in the axial direction, and the profiles of velocity and turbulence quantities are extracted at the burner exit plane, x/D of 0, as in [11]. The thermochemical composition at the inlet boundary is prescribed in one of two ways: the first way is to define the composition of the burned streams (that is, the pilot and coflow) to be at chemical equilibrium; the second way is to define the composition of those streams based on a fully burnt laminar flame. The composition of the fully burnt laminar flame is obtained from a Chemkin calculation using the 44-species UCSD mechanism [39] and considering full multicomponent transport and thermal diffusion. The resulting boundary conditions are presented in detail in Table 3.

2.3 The Effect of Molecular Diffusion in the RANS-PDF Calculations

It is found in [11] that the mixing layer between the pilot and the coflow is predicted to evolve much more slowly in the calculations than observed in the experiments. Because the pilot and the coflow bulk velocities are both low and the molecular diffusivity of each stream is large, the observed discrepancy is most likely due to molecular diffusion. In turbulent flames, molecular diffusion is usually small compared to turbulent diffusion, so it is typically neglected in these types of RANS-PDF calculations. To investigate the first-order effects of molecular diffusion in these flames, a simple random walk model is implemented into this method.

In this simple model for molecular diffusion, two additional terms are added to the equation for advancing a particle's position in physical space as illustrated in Eq. 1:

$$d\mathbf{X}^* = \mathbf{U}^* dt + \left(\frac{1}{\langle \rho \rangle} \nabla \left(\langle \rho \rangle \alpha \right) \right)^* dt + \sqrt{2\alpha} d\mathbf{W} \tag{1}$$

where $d\mathbf{X}^*$ is the change in a particle's position, $\mathbf{U}^*$ is the current particle velocity, dt is the time step, $\langle \rho \rangle$ is the volume-weighted mean density, $d\mathbf{W}$ is an increment in an isotropic, vector-valued Wiener process, and α is the mass-weighted cell mean molecular diffusivity which depends on position. The second and third terms on the right-hand side are evaluated based on interpolation of the fields onto the particle's

current position. The first additional term in Eq. 1 represents the mean drift due to molecular diffusion, while the last term represents a random-walk term. It is very important to note that this simple model results in a spurious production of variance due to the random-walk term [38, 40]. Therefore, this model is only used to examine the first-order effects in the RANS-PDF calculations, and more sophisticated models are discussed and used later in this work.

Before examining this model's effects on the PPJB calculations, several tests are performed to verify its correct implementation. Each test consists of a two-stream laminar mixing layer with distinct species mass fractions specified in each stream; the coordinate system, density, and diffusivity are varied among the tests to verify each component of the model. Four test cases are considered, and are outlined in Table 4.

The results from the test cases are compared to solutions from the commercial CFD tool Fluent and to analytical solutions where possible. Each solution is investigated for sufficient numerical accuracy by varying the grid size, the number of particles per cell, and the duration of time-averaging. The results of these verification tests are summarized in Figure 2, where lateral and radial profiles of species mass fractions from test cases A and D are shown. The results from all the test cases are found to be in good agreement with the results from other solution methods; next, the effect of this model is examined in the calculations of the PPJB flames.

To implement the simple model based on Eq. 1, the molecular diffusivity must be defined. In this simple implementation of molecular diffusion, the Lewis number is taken to be unity, so that the molecular diffusivity is simply equal to the thermal diffusivity. For all the compositions realized throughout a flamelet generated manifold (FGM) discussed later in this work, the thermal diffusivity is evaluated using Chemkin, and a curve-fit is constructed as a function of temperature as

$$\alpha(T) = \alpha_0 \left(T/T_0\right)^b, \tag{2}$$

where α is the molecular diffusivity, and T is the mass-weighted cell mean temperature. The reference temperature, T_0, is defined as 300 K, where the reference diffusivity, α_0, is equal to 2.24×10^{-5} m^2/s. The exponent, b, is obtained from the curve-fit, and is equal to 1.71. Comparisons of the transport properties evaluated on the FGM to the curve-fits are presented later in this work.

Presented in Figure 3 is a comparison between two calculations and the experimental measurements for the time-averaged mass-weighted mean temperature and pilot mixture fraction for flame PM1-50. In these flows, three streams are considered, and a mixture fraction is associated with each stream. The mixture fraction represents the fraction of mass originating from that stream, and it is defined here based on a linear combination of the elemental mass fractions, H, O, and C. The first set of calculations shown in Figure 3 is essentially identical to that in [11], and the second set of calculations is identical, except with the additional terms in Eq. 1 to model the molecular diffusion, and the diffusivity evaluated through Eq. 2.

There are three important observations from the comparison of these two calculations. The first is that the calculations with molecular diffusion have much more accurate profiles of mean scalars (such as temperature and pilot mixture fraction) in the pilot-coflow mixing layer. The results convincingly show that molecular diffusion is important in this region of the flow, due to the low velocity of the pilot and coflow streams. This marks a significant difference between the PPJB flames and other turbulent jet flames previously studied. The second important observation is that the overall reaction progress of the jet is not significantly affected by the

new treatment of molecular diffusion. This occurs mainly because the pilot-coflow mixing layer is sufficiently far from the central fuel jet; by the time the pilot-coflow mixture interacts with the central jet fluid, the pilot and coflow are already well-mixed. A third observation, which will be presented and discussed more in detail in Sec. 3.3, is that the spurious variance introduced by this random-walk model is large and is clearly evident in the radial profiles of the RMS of temperature and chemical species, up to at least x/D of 15.

2.4 The Effect of the Temperature at the Inlet Boundary Condition

Having examined the first-order effect of molecular diffusion on the PPJB calculations, a second important aspect of the model is next examined, namely, the temperature prescribed at the inlet boundary. One deficiency observed in previous calculations of the PPJB flames is an overpredicted temperature in the coflow near the burner exit, by as much as 300 K [10, 11, 15–17]. This discrepancy occurs because, in the experiments, the hot coflow transfers heat to the cold unreacted pilot stream, and this heat transfer is not taken into account in these calculations. The heat loss has been investigated in some previous studies [10, 11], but the results have been not been convincingly improved, possibly due to the neglect of molecular diffusion in those former calculations. In [18], the heat loss is accounted for, but it is specified empirically from an extrapolation of the measurements at x/D of 2.5. The purpose of this part of the study is to perform a thorough analysis of this boundary condition, and to examine the sensitivity of the calculations to it. Because molecular diffusion is now included, much better agreement is obtained in the pilot-coflow mixing layer.

To model the heat transfer between the pilot and coflow, the commercial CFD tool Fluent is used. The domain of these calculations extends from $x/D = -100$ to $x/D = 100$, as in the previous calculations used to obtain the boundary conditions. At the region from $x/D = -100$ to 0, referred to as the upstream region, conjugate heat transfer is modeled between the cold pilot fluid and the hot coflow through the pilot-coflow wall. A detail of the upstream region is shown in Figure 4. The heating takes place over the entire length of the upstream region, and the thermal boundary layer is fully developed by the jet exit plane at x/D of 0. This boundary condition is implemented into the RANS-PDF calculations by extracting the temperature and density at $x/D = 0$, as well as the velocity and turbulence properties as before. In the RANS-PDF calculations, the density is prescribed at the inlet from these conditions, and the sensible enthalpy is obtained from the species mass fractions and temperature.

Shown in Figure 5 is a comparison between the calculations with and without heat loss in the coflow. Three important observations can be made from this figure. The first is that the time-averaged mass-weighted mean temperature is predicted with much greater accuracy when the heat transfer is accounted for, as would be expected. With an adiabatic coflow, there is a 300 K temperature disparity near the pilot-coflow mixing layer, which propagates downstream even farther than x/D of 25, the measurement location farthest downsteam. The agreement in the mean temperature between the experimental measurements and calculations with heat transfer is excellent near the burner exit at x/D of 2.5. The agreement degrades slightly going downstream, which is most likely a result of the turbulence modeling of the spreading of the pilot stream. This is confirmed by examining the pilot mixture fraction, which spreads slightly faster in the calculations compared to the experiments.

The second important observation from Figure 5 is that the calculations with

heat transfer in the boundary conditions have profiles of the time-averaged mass-weighted mean pilot mixture fraction which are shifted from the previous calculations toward the centerline, in much better agreement with the experimental data. This occurs primarily due to the inclusion of the chamfered edge of the pilot-coflow wall in this boundary condition formulation, and not necessarily due to the heat transfer itself. The chamfered edge results in a slightly larger radial velocity toward the centerline, and hence, slightly faster entrainment of the coflow. Other calculations which do not account for the chamfered edge [10, 11, 15–18] display similar behavior, and could benefit slightly from that addition in the boundary condition. The last observation from Figure 5 is that the overall combustion of the fuel from the central jet is not significantly affected by the temperature treatment at the inlet boundary condition, for this range of temperatures. By the time the jet mixes with the fluid from the pilot-coflow mixture layer, it is already sufficiently well-mixed. The findings agree with those of [11], where reducing the coflow temperature in PM1-200 to as low as 1200 K did not significantly impact reaction progress.

2.5 Comparison of Combustion Modeling Methodologies

In the next part of this work, a flamelet-generated manifold (FGM) [41, 42] is applied to model the combustion in the PPJB. The purpose of doing so is two-fold: firstly, to reduce the computational cost, particularly for the more expensive LES-PDF studies; and secondly, to examine the sensitivity of the PPJB calculations to the combustion modeling. These studies provide a direct comparison between calculations with detailed chemistry and calculations with simplified combustion models.

For this particular application of FGM, three variables are considered: a mixture fraction of both the jet and pilot streams, ξ_j and ξ_p, and one reaction progress variable, taken here to be the sensible enthalpy, h_s. A grid is constructed in the ξ_j and ξ_p mixture fraction space; for each point in the grid, a chemical composition corresponding to inert mixing of the three streams is formed based on the values of ξ_j and ξ_p at that point. From this composition, a freely-propagating laminar flame is computed for each value of mixture fraction in the grid. In the RANS-PDF calculations, both mixture fractions have no source term. The source term for the sensible enthalpy, $\dot{h_s}$, is evaluated by performing a table look-up from the current values of ξ_j, ξ_p, and h_s and interpolating. The change in h_s over one time step is then computed from simple Euler integration, with integration performed over n_{sub} sub-steps within the current time step as shown in Eq. 3:

$$h_s(t+\Delta t) = h_s(t) + \int_t^{t+\Delta t} \dot{h_s}\left(\xi_j(t'), \xi_p(t'), h_s(t')\right)\, \mathrm{d}t'. \tag{3}$$

A second manifold is constructed by the same process as above, but instead of computing a laminar flame, an auto-ignition calculation is performed for each composition formed by inert mixing of the three streams. The purpose of this second manifold is to examine the importance of diffusive effects, and to facilitate comparisons between the two sets of boundary conditions from Table 3. For each of these two manifolds, calculations are made using the 44-species UCSD mechanism [39] and the 111-species USC-Mech-II chemical mechanism [43]. The first of the manifolds, assembled from laminar flame calculations, is denoted as FGM-LF; the second, assembled from auto-ignition calculations, is denoted as FGM-AI.

The numerical accuracy of this method is affected by the size of the grid in

ξ_j, ξ_p, and h_s, the number of time steps over which the numerical integration is performed, and accuracy to which the flamelets are computed. Convergence studies are performed over all of these parameters, and an error in the ignition delay time, ϵ_t, is defined for each configuration by

$$\epsilon_t = \left| t_{ig}^{FGM} - t_{ig} \right| / t_{ig}, \tag{4}$$

where t_{ig}^{FGM} is the ignition delay time based on that configuration of the FGM, and t_{ig} is the ignition delay time computed directly from a laminar flame calculation (or an auto-ignition calculation, in the case of the second manifold) of sufficient numerical accuracy computed using Chemkin. The ignition delay time is defined here as the time taken for the sensible enthalpy of a particle starting from the unburned composition to increase by 50% of the total change in sensible enthalpy. Accuracy tests are conducted using a time step of 10^{-6} seconds, which is near the time step used in the calculations. The time evolution of sensible enthalpy and its time rate of change for a value of (ξ_j, ξ_p) around the most sensitive region of mixture fraction space, $(0.47, 0.50)$, in one of the accuracy tests is illustrated in Figure 6. This figure illustrates the consistency between the solution computed using appropriate accuracy in a Chemkin calculation and the solution computed from interpolating in ξ_j, ξ_p, h_s, and time in the FGM.

The accuracy test of the grid size and interpolation is illustrated in Figure 7. Three grids are defined, FGM-16, FGM-32, and FGM-64, and have, respectively, 16, 32, and 64 grid points in each dimension. For a large number of points inside the range ($0.44 \leq \xi_j \leq 0.56$) and ($0.44 \leq \xi_p \leq 0.56$), ϵ_t is measured. The convergence tests shown in Figure 7 reveal that the error decreases as the grid is refined. Secondly, the error is lowest at the locations near the grid nodes. This study shows that the error from the grid discretization is larger than the error associated with the time sub-step. A grid size of $32 \times 32 \times 100$ in ξ_j, ξ_p, and h_s, and a value of n_{sub} of 4 yields a maximum ϵ_t of about 0.10, and the results from calculations of the PPJB are insensitive to numerical parameters giving greater accuracy. Therefore, these are the numerical parameters used in this study of the FGM.

Figure 8 shows the results of using both FGM-AI and FGM-LF with the USCD mechanism [39] to model the combustion in PM1-50. The results obtained with these models are compared to results obtained using detailed chemistry with the two sets of boundary conditions described in Table 3; for FGM-AI, the results are compared to those with detailed chemistry and equilibrium boundary conditions, and for FGM-LF, to those with laminar flame boundary conditions with heat loss in the coflow. The results obtained with FGM-AI are in remarkably good agreement to the results obtained using detailed chemistry for the mean mass fractions of major species such as CH_4 and CO_2. For the mean mass fractions of CO and OH, the FGM-AI calculations are generally within 10% of the values from the calculation with detailed chemistry; FGM-AI slightly overpredicts the mass fractions of these species, which would suggest that diffusive processes are responsible for the slightly lower mass fractions of CO and OH observed in the calculations with detailed chemistry. The performance of FGM-LF is similar in terms of the mean mass fraction of CH_4 and CO_2, and is slightly more consistent with the calculations with detailed chemistry than that of FGM-AI, in terms of the mean mass fractions of CO and OH. Figure 8 also shows that the differences between FGM-AI and FGM-LF are caused by both the combustion modeling as well as by the different boundary conditions. This thorough comparison of the simplified combustion models to detailed chemistry shows that the combustion in these calculations is

not particularly sensitive in terms of the major species such as CH_4, O_2, H_2O, and CO_2, but for the species in smaller concentrations, like CO and OH, the results are slightly more sensitive to the combustion modeling.

The same calculations are performed in PM1-200, and the agreement in the mean and RMS species mass fractions between the calculations using detailed mechanisms and those using FGM-based modeling is of similar quality to that in PM1-50. However, the reaction progress in the calculations of PM1-200 is overpredicted using both chemistry models, so no strong conclusions about the adequacy of FGM-based models in PM1-200 can be drawn from that comparison.

With respect to other studies of the PPJB using simplified combustion modeling [18], these comparisons assist in validating the use of those models for the major species and density, and provide an explanation for the observed discrepancies in the mass fractions of CO and OH in those studies. One deficiency of the FGM investigated here is the inability to account for the heat loss in the coflow stream, which is one advantage of the approach used in [18]. This could be accounted for by adding an additional variable into the formulation. However, the objective of this part of the study is to describe the reaction progress as simply as possible; based on the previously discussed findings regarding the effect of the coflow temperature on the overall combustion in the flame, the results using the FGM provide acceptable results. The FGM-LF model is selected to be used in the first LES-PDF in this work, before advancing to the calculations with detailed chemistry.

3. LES-PDF Calculations

The results from Sec. 2 show how the treatment of molecular diffusion, inflow boundary conditions, and chemistry modeling affect the calculations of the PPJB flames in the context of the RANS-PDF method, and the results demonstrate much more accurate calculations of PM1-50 than any previous study. However, none of these components of the modeling yield calculations of PM1-150 and PM1-200 in much better agreement to the experimental data. Therefore, the more complete modeling methodology of LES-PDF is next considered so that the effects of molecular diffusion can be examined in greater detail, and with a more complete level of turbulence modeling.

The LES-PDF methodology is a hybrid method in which large-eddy simulation (LES) and probability density function (PDF) methods are used together to model a turbulent reactive flow. In LES, the large scales of the turbulence are resolved, and the small scales must be modeled. Since the large scales contain most of the kinetic energy of the flow, most of the large-scale features of the flow can be resolved. However, most chemical reaction occurs at very small scales, so the sub-model used to describe this process is a very important part of the overall model. There are a number of existing sub-models for chemical reaction, among which is the PDF method. The primary advantage of the PDF method is that chemical reaction can be treated exactly through elementary reactions in a detailed chemical mechanism, and therefore can represent turbulence-chemistry interactions most effectively. Various formulations of the LES-PDF methodology have recently been used to perform calculations of turbulent flames [44–50]. The approach taken in this work is based on that used in [49, 50] and is next described.

3.1 Computational Methodology for the LES-PDF Calculations

The LES-PDF approach used to study these flames is based on the LES framework of self-conditioned fields [51] and the two-way coupled hybrid method developed in [49, 52, 53]. The LES transport equations for mass and momentum are solved with overall second-order accuracy using the methodology of [54]; continuity is enforced through solving the pressure Poisson equation. The turbulent viscosity is computed using an algebraic sub-grid scale model [55], and the turbulent diffusivity is computed from the turbulent viscosity using a turbulent Schmidt number of 0.4. The effect of the turbulent Schmidt number on the calculations has been examined in PM1-150, and it is found that a 25% variation in this parameter has little effect on the calculations.

An additional equation for the specific volume is solved in the LES, and the source term for this equation is obtained from the particle solver [56]. The LES solver provides the particle solver with the filtered velocity, density, turbulent viscosity, turbulent diffusivity, molecular diffusivity, and mixing frequency.

As opposed to the RANS-PDF method, which considers the joint PDF of velocity, turbulence frequency, and compositions, the LES-PDF method used here considers the joint PDF of compositions. In the particle solver, the particles evolve in physical space and in composition space. A splitting scheme with second-order accuracy [52] is used to advance the particles over each time step. The quantities from the LES solution are used to advance the particles in physical space as developed in [53] and also used in [49, 50]. The particle composition evolves by Eq. 5,

$$\frac{d\phi^*(t)}{dt} = -\Omega_M^* \left(\phi^* - \tilde{\phi}^*\right) + \left(\frac{1}{\bar{\rho}}\nabla\left(\bar{\rho}\tilde{\alpha}\nabla\tilde{\phi}\right)\right)^* + \dot{S}(\phi^*), \tag{5}$$

where ϕ is the particle composition vector, Ω_M is the mixing frequency, $\bar{\rho}$ is the filtered density, $\tilde{\alpha}$ is the mass-weighted filtered diffusivity, and $\dot{S}$ is the reaction source term. The superscript "$*$" denotes a quantity evaluated at the particle position. The first two terms in Eq. 5 represent the modeling of mixing, the first term being molecular mixing, and the second term being molecular transport. This treatment of molecular diffusion allows differential diffusion to be accounted for in the model, and it produces no spurious scalar variance [38, 40]. The mixing frequency is computed from Eq. 6,

$$\Omega_M = C_M \left(\tilde{\alpha} + \alpha_T\right)/\Delta^2, \tag{6}$$

where α_T is the turbulent diffusivity, Δ is the filter width, and the constant mechanical-to-scalar timescale ratio, C_M, is set to a value of 5.0 for the base case, as in [50]. The constant C_M is often denoted by C_ϕ. However, here the symbol C_M is used to differentiate this constant from the mechanical-to-scalar timescale ratio used in the RANS-PDF calculations, C_ϕ.

The third term in Eq. 5 represents chemical reaction, and here it is evaluated using the ISAT storage and retrieval algorithm [36, 37] for computational efficiency. Upon completion of the current time step, the particle solver then provides the LES solver with the volume-weighted mean density, mass-weighted mean temperature, and source term for specific volume. The two-way coupled hybrid method proceeds in this way throughout the calculation. After a statistically stationary state has been reached, the statistics of interest are time-averaged until temporal convergence is attained.

3.2 Computational Configuration of the LES-PDF Calculations

The computational domain for the LES-PDF calculations is a cylinder of size $75D \times 25D \times 2\pi$ in the axial, radial, and circumferential directions. A sketch is shown in Figure 9. At the pilot and coflow inflow plane, the velocity boundary conditions are prescribed based on the laminar flow identical to the mean velocity used in the RANS-PDF calculations. At the jet inflow plane, the velocity is taken from a separate turbulent pipe-flow simulation at the appropriate value of Re. The same chemical mechanism used in the RANS-PDF calculations, the 16-species ARM-1 mechanism [35], is used to describe the detailed chemical kinetics in the base case. The compositions provided at the inlet are taken from the laminar flame inflow conditions in Table 3; however, the temperature and density at the inlet are specified using the boundary conditions with heat loss in the coflow. The viscosity is obtained from a curve-fit to data from the FGM. For each composition realized in the FGM, the kinematic viscosity, ν, is evaluated with Chemkin, and a curve-fit is made as a function of temperature by

$$\nu(T) = \nu_0 \left(T/T_0\right)^b, \tag{7}$$

where the reference temperature, T_0, is 300 K, and the reference viscosity is, ν_0, 1.60×10^{-5} m^2/s. The exponent b is obtained from the curve-fit and is equal to 1.69. The base case is set up with unity Lewis number in all the species, and the diffusivity is evaluated in the same way as described for the RANS-PDF equations, using Eq. 2 and all the same parameter values. The case of differential diffusion is discussed in Sec. 3.4.1. Figure 10 shows both the molecular diffusivity and the kinematic viscosity as evaluated on all the compositions throughout the FGM as functions of temperature. Both the viscosity and the diffusivity are well-described as a function of only the temperature, and the curve-fits provided to Eq. 2 and Eq. 7 represent these transport properties well. The calculations are performed for all four PPJB flames using this formulation of the base case. Figure 11 shows contours of instantaneous resolved mass fraction of CO from these calculations. As the jet velocity increases, the coflow and pilot streams are more rapidly entrained by the central jet, and the length of the flame generally increases.

3.3 Numerical Accuracy of the LES-PDF Calculations

In the LES-PDF calculations, the primary sources of numerical error include the grid discretization, the finite number of particles, the finite duration of time-averaging, and the error tolerance associated with the chemistry tabulation in ISAT. All of these parameters are investigated through convergence studies, and it is found that the largest source of numerical error is the grid resolution. The grid resolution is especially important in the context of LES, where the resolution directly affects the filter width, and thus, how much of each quantity is either resolved or unresolved. A number of different criteria exist for determining the grid quality for a LES, and there is still no universal standard criterion by which to assess the quality. This remains an important topic for future study, but is beyond the scope of this work, other than to ensure that the investigated quantities do not exhibit significant sensitivity to the grid resolution beyond that used. Therefore, to establish the level of numerical accuracy of the calculations with respect to the grid resolution, several convergence studies are performed on progressively refined grids. The statistics of interest for each calculation are then compared to those statistics on the most highly resolved grid and the error for each statistic on each

grid is measured.

The first set of convergence studies is conducted on a non-reacting flow based on the same configuration as the PPJB. Only a single LES is necessary for these calculations; there is no chemical reaction source term, and the density can be obtained directly from the mixture fractions. The grid sizes used for these calculations are shown in Table 5. The relative number of cells in each direction is chosen based on the configuration which yields the most rapid grid convergence. The results of this convergence study are summarized in Table 5 for the flow NR-200, which is based on PM1-200, the PPJB flame with the highest jet bulk velocity. Among all the flows considered in this work, NR-200 has the largest numerical error from grid resolution. The error in the time-averaged statistics for each calculation is computed by taking the difference between the statistics in that calculation and the statistics on the most highly resolved grid; the maximum error in time-averaged mass-weighted statistics at an axial location of x/D of 30 is shown in Table 5. On grid G4, The maximum error at x/D of 30 is about 5% for the resolved mean axial velocity, 1% for RMS of the resolved axial velocity, 4% for the resolved mean jet mixture fraction, and 1% for the RMS of the resolved jet mixture fraction.

A grid convergence study is also performed for the reacting flows. The results of the grid convergence study for PM1-50 are also summarized in Table 5. These reacting flow calculations have considerably less numerical error from the grid resolution than do the non-reacting cases; due to the heat-release in the reacting flows, the pilot and coflow streams are not entrained as strongly into the jet as they are in the non-reacting flows. Grid G3 exhibits errors of around 2% for the mean and RMS of the resolved temperature and jet and pilot mixture fractions. Figures 12 (a) and (b) show the radial profiles of the mean and RMS statistics for this convergence study. Besides grid G1, the other grids all yield reasonably similar statistics. The largest numerical errors occur in the RMS statistics of the resolved scalar fields around the centerline. It is observed that as the jet velocity increases, the requirements for numerical accuracy also increase. Grid G3 is used as the base case grid for the calculations of PM1-50, while both grids G3 and G4 are used to perform calculations of the other flames, PM1-100, PM1-150, and PM1-200.

Figures 13 (a) and (b) show the mean and RMS statistics in the base case calculations of PM1-50. The figures demonstrate good consistency between the mean scalar fields in the RANS-PDF and LES-PDF calculations, and an improvement in the calculations of the RMS statistics in the LES-PDF calculations in the near-field region of the pilot-coflow mixing layer. The use of the boundary condition with heat loss significantly improves the calculations of the temperature throughout the flame, and do yield a small improvement in the amount of fuel burned near the centerline farther down in the flame, as is also seen in the RANS-PDF study. The total RMS as obtained from the particles and is shown in Figure 13 (b). At the jet-pilot interface, the unresolved component of the RMS accounts for about 30% of the total RMS at x/D of 2.5, and about 20% of the total RMS at x/D of 7.5. Beyond x/D of 7.5, the unresolved component of the RMS is generally less than 10% of the total RMS.

3.4 The Effects of Modeling Molecular Diffusion in the LES-PDF Calculations

In LES-PDF, modeling is required to treat the conditional diffusion term in the PDF transport equation. This is done through the mixing model described above in Eqs. 5 and 6, and entails one of the largest sources of modeling uncertainty in the calculations. For that reason, a thorough investigation is performed with

respect to two aspects of the mixing model. The first aspect investigated is the effect of differential diffusion, and the second aspect investigated is the value of the parameter, C_M, which represents the mechanical-to-scalar timescale ratio.

3.4.1 The Effects of Differential Diffusion

A major assumption made in the base-case calculations, as well as in the previously discussed RANS-PDF calculations, is that the Lewis number is unity for all chemical species. In reality, this is not the case, as lighter species generally have a higher diffusivity, and heavier species generally have a lower diffusivity. In the configuration of the PPJB, there are significant concentrations of light species such as OH, H_2, and H in both the pilot and coflow. Furthermore, it has already been shown that molecular diffusion is important in modeling the pilot-coflow mixing due to the low velocities and high temperatures of the pilot and coflow streams. Therefore, a careful investigation of the effect of differential diffusion in these flames is important in understanding their behavior.

Figure 14 shows the molecular diffusivity of each chemical species in the ARM-1 mechanism evaluated throughout the entire FGM manifold, as well as the thermal diffusivity. From the figure, it is clear that there is a large range in the diffusivity of the different species. The lightest species, H, has a diffusivity larger than the thermal diffusivity by a factor of about eight, and that of H_2 is about four times greater than the thermal diffusivity. Figure 14 also shows that the diffusivity of each species is well-described as a function of only the temperature.

Using the diffusivities evaluated on the FGM, as shown in Figure 15, curve-fits are made as functions of temperature in the form of Eq. 8,

$$\alpha^i(T) = \alpha_0^i \left(T/T_0\right)^{b^i} , \tag{8}$$

which is identical in form to Eq. 2, but the superscript "i" denotes a quantity for species i. The values obtained from the curve-fit for each species are shown in Table 6.

A comparison between calculations with and without differential diffusion in flame PM1-50 is shown in Figure 15. The general conclusion is that the effects of differential diffusion are limited to the near-field of the flow (around x/D of 2.5 and 7.5) and to the species H_2, CO, and OH, as well as other species in smaller concentrations. There is interesting behavior observed in the near-field of the flow to which the differential diffusion gives considerable insight. The most notable difference in the calculations with and without differential diffusion is in the mean mass fraction of CO. When differential diffusion is included in the calculations, the amount of CO in the pilot-coflow mixing layer decreases to a value closer to that measured. This occurs not because of the diffusivity of CO (which is roughly equal to the thermal diffusivity), but rather because of the diffusivity of the other light species in the coflow and pilot. When differential diffusion is included, a greater concentration of these lighter species react with CO to form CO_2 in the pilot-coflow mixing layer, and thus the mass fraction of CO there is reduced. In addition to flame PM1-50, the same study of differential diffusion is applied in flame PM1-150; this yields a similar effect, but of smaller magnitude. This observation is reasonable because the pilot-coflow region is much smaller in flame PM1-150 due to the more rapid entrainment by the jet, and the effect of differential diffusion is primarily limited to this region.

3.4.2 The Effect of the Model Constant C_M

The second important aspect of modeling molecular diffusion is the value of the parameter C_M. The mixing frequency, from Eq. 6, is directly proportional to C_M.

In previous RANS-PDF calculations of the PPJB, it is found that the value of C_ϕ had two main effects: larger values of C_ϕ result in decreased scalar variance [10, 11] and a decreased spreading rate of the jet [11]. In this study, the value of C_M is varied over values of $\{2, 5, 10, 20, 50, 100\}$ for flame PM1-150. The numerical implementation with a second-order scheme where the boundedness for ϕ is guaranteed [40, 52] ensures that there are no numerical accuracy or stability issues for large values of C_M. Contour plots of the instantaneous CO mass fraction from this parameter study are shown in Figure 16. As C_M increases, the flame length increases and the spatial variance of the resolved fields decreases.

Figure 17 shows the effect of C_M on the fraction of the time-averaged mass-weighted total RMS of the CO mass fraction which is unresolved. In the base case calculations of PM1-150, the maximum unresolved RMS is about 30% of the total RMS in the near-field (from $x/D = 0$ to $x/D = 15$), and less than 20% beyond $x/D = 15$. As C_M increases, the unresolved portion of the total RMS decreases; for $C_M \geq 20$, the unresolved RMS is less than 5% of the total RMS at all locations at which the total RMS is significantly large (values of the total RMS at least 2% of the RMS at the centerline). The observations about the unresolved RMS made for the CO mass fraction generally hold true for the mass fractions of other species. A second observation from Figure 17 is that as the constant C_M increases, the total RMS decreases and its distribution in physical space changes. As C_M increases, the peak in the total RMS of the CO mass fraction moves out from the centerline. This is a result of the changing shape of the flame caused by C_M. With larger C_M, the flame has more homogeneity near the centerline due to the increased intensity of mixing. Most of the strong gradients in physical space move outward from the centerline, and most mixing takes place at these locations.

The results of this parameter study are illustrated quantitatively in Figures 18 and 19. Figure 18 shows the time-averaged mass-weighted mean of the resolved temperature and species mass fractions for values of C_M of 5, 20, and 50. As C_M increases, the fuel mass fraction increases at x/D of 15 and 30. When C_M is increased to around 50 or 100 (not shown), very good agreement in the overall reaction progress is obtained by x/D of 15 and 30. This includes both the mean and RMS statistics. However, for the near-field region, smaller values around 5 or 10 yield results in better agreement with the experimental measurements. For axial locations beyond x/D of 30, it appears that even larger values of the mixing frequency are required; however, simply using a larger value of C_M does not improve the accuracy of the calculations beyond x/D of 30 due to the adverse effect of larger values of C_M in the near-field of the jet.

Increasing the mixing frequency (via increasing C_M) effectively reduces the residual variance. Figure 19 shows that the unresolved portion of the RMS is significant in the near-field when C_M is 5, and the total RMS is overpredicted for the mass fractions of all these species in the near-field. As C_M increases, the unresolved portion of the RMS decreases, and larger values of C_M produce results of the total RMS much more consistent with the experimental data.

Figure 20 shows particles from a single row of cells in this parametric study. When C_M is 5, the base case, there is a very large amount of residual variation in the temperature, with variation as large as 500 K near the jet-pilot reaction zone. As C_M increases, this residual variation in the particle quantities clearly decreases, as shown in Figure 20. When C_M is 20, the maximum variation in the pilot-jet reaction zone is only about 300 K, and when C_M is increased to 100, the maximum variation at this location further diminishes to about 200 K. The framework used in the LES calculations in [15] should be examined carefully in light of the significant amount of subgrid-scale variation observed here.

4. Comparison of RANS-PDF and LES-PDF for all Flames

One of the major deficiencies of previous calculations is the overprediction of the reaction progress, particularly in the flames with higher jet velocities (i.e., PM1-150 and PM1-200) [10, 11]. Even in calculations of PM1-100, all previous studies report the flame length being calculated as shorter than measured experimentally [10, 11, 15–18]. This discrepancy is generally manifested in the calculations by accurate mean mixture fractions, underpredicted mass fractions of fuel and oxidizer, and overpredicted mass fractions of products (CO_2 and H_2O) and mean temperature. Considering that one of the main features of these flames is the reduced reaction progress in PM1-150 and PM1-200 around x/D of 30, the ability to predict the reaction progress rate accurately at this location is extremely important in assessing the quality of the numerical methods used to model these flames.

Some previous studies [10, 11] identify the mixing models as the most likely cause of the observed discrepancy in reaction progress. However, neither of those previous studies shows, quantitatively, that a different model of mixing yields the observed reaction progress in PM1-150 or PM1-200. One of the major reasons is that, in those previous RANS-PDF studies based on the joint PDF of velocity, turbulence frequency, and composition [11], variation of C_ϕ affected not only the reaction progress, but also the scalar flux. Thus, the jet spreading rate is altered by the change in C_ϕ and quantitative agreement with the experimental measurements is not achieved for larger values of C_ϕ. However, in the LES-PDF parameter study of C_M performed in this work, the scalar flux is not directly affected by the value of C_M. For sufficiently large C_M, excellent quantitative agreement can be achieved at x/D of 30 in PM1-150 for mean and RMS statistics. These results demonstrate a clear link between the mixing frequency and the reaction progress. Given that such large values of C_M are required to achieve the correct reaction progress, this study is highly suggestive that the mixing frequency in this region of the PPJB flames is dominated by scales other than those in Eq. 6.

To quantify the amount of reaction progress in a way that allows an efficient comparison to experimental data, a mean Fuel Consumption Index (FCI) is introduced, which is defined as

$$FCI(x,r) = 1 - \frac{\langle Y_{fuel}(x,r)\rangle / \langle \xi_j(x,r)\rangle}{Y_{fuel}(x_0,r_0)/\xi_j(x_0,r_0)}, \tag{9}$$

where Y_{fuel} is the mass fraction of the fuel, and x_0 and r_0 are the axial and radial location of the origin of the fuel stream. The quantity FCI represents the mean mass fraction of fuel that has burned relative to the amount the jet has been mixed. So, a value of 0 represents an entirely unburned composition, and a value of 1 represents a fully burned composition. One disadvantage of using the FCI as defined in Eq. 9 is that it is only defined on the centerline, so it only represents a small portion of the flow domain and it is subject to considerable statistical error in the measurements. Therefore, comparisons of this quantity must consider these factors as well. The experimental data demonstrates errors around 10-20% in FCI at some locations, based on unrealizable mass fractions and mixture fractions.

Figure 21 shows the evolution of this quantity along the jet centerline in the RANS-PDF calculations, LES-PDF calculations, and experiments. The obvious deficiency observed in many of the previous studies, as well as in this study, is observable in Figure 21 as the excessively rapid consumption of fuel in the calculations of PM1-150 and PM1-200. The improvement obtained through larger values of C_M is observable in Figure 21 (c) for PM1-150, although it is clear that there is still room for improvement in the prediction of this quantity.

The primary benefits of using the LES-PDF methodology over RANS-PDF in this work have been to model the molecular diffusion without spurious variance production, to examine the effect of differential diffusion, and to investigate the effect of C_M without significant effect on the scalar flux. The more complete turbulence modeling of LES-PDF yields slightly more accurate spreading of the pilot stream, and there is no dependence on turbulence model parameters such as $C_{\omega 1}$; but generally in this jet flow of simple geometry, both the RANS-PDF and LES-PDF calculations yield similar descriptions of the velocity fields. The computational costs of each approach is outlined in Table 7 for various case configurations of PM1-50. The LES-PDF calculations are generally more expensive by a factor of about 20 compared to the RANS-PDF calculations. So, in this flow, the advantages of LES-PDF are somewhat under-realized; in more practical applications to combustion devices, where the flow is much more complex, the benefits of using LES-PDF would provide greater justification to its higher cost.

5. Conclusions

In this study, both RANS-PDF and LES-PDF computational methodologies have been employed to investigate thoroughly the PPJB flames. The most crucial aspects of modeling these flames successfully have been identified in this work in the following five conclusions:

(1) Molecular diffusion is important in the pilot-coflow region of the near-field. This process is implemented into the RANS-PDF method using a crude random-walk model and is tested for accuracy. The resulting mean fields of mixture fractions, temperature, and species are much improved through these calculations. The spurious production of variance from the random walk model, however, results in poor predictions of the RMS fields near the pilot-coflow mixing layer. A newly developed implementation of molecular diffusion [38, 40] is used in the LES-PDF calculations, which yields much improved RMS statistics without a spurious production of variance.

(2) A simple FGM three-variable chemistry model based on two conserved scalars (mixture fractions) and one reaction progress variable is implemented and tested for accuracy. The results indicate predictions of fuel consumption in good agreement with calculations using detailed chemistry for all four PPJB flames. The mass fractions of major species in these flames appear relatively insensitive to the chemistry modeling, as noted in previous studies. Comparisons to identical calculations using full chemistry give a good quantitative comparison between the two approaches. Although good agreement between the calculations with detailed chemistry and FGM-based chemistry is obtained for all four PPJB flames, the reaction progress is overpredicted in PM1-150 and PM1-200. Therefore, strong conclusions about the accuracy of the FGM-based approach hold only for PM1-50 and PM1-100.

(3) Boundary conditions considering the heat loss in the coflow, the curved geometry of the pilot-coflow interface, and compositions taken from fully burnt laminar flames in the pilot and coflow streams, yield calculations in very good agreement with the measurements near the burner exit. The heat loss has a small effect on the amount of fuel consumed downstream. The curved geometry of the pilot-coflow interface shifts the pilot and coflow mixture fractions toward the centerline. The laminar flame boundary conditions yield slightly better predictions of CO and OH in the pilot than

compared to equilibrium conditions, but do not significantly affect the mass fractions of major species throughout the flame.

(4) For the low velocity flames (PM1-50 and PM1-100), good results can be obtained through both RANS-PDF and LES-PDF methods using the above boundary conditions and treatment of molecular diffusion. This is quantified by reasonable agreement in the mean and RMS statistics of temperature and species mass fractions throughout all measured locations.

(5) For the high velocity flames (PM1-150 and PM1-200), the RANS-PDF calculations overpredict the reaction progress beyond x/D of 15, as observed in previous studies of these flames [10, 11]. The LES-PDF calculations yield excellent agreement in the mean and RMS statistics of temperature and species mass fractions at x/D of 15 and 30 when the value of C_M is increased to around 50 or 100, whereas previous RANS-PDF studies of C_ϕ did not achieve quantitative agreement with larger C_ϕ due to the affect of C_ϕ on the scalar flux, the level of turbulence modeling, and the boundary conditions. The LES-PDF calculations provide a strong link between the larger values of mixing frequency, and the observed improvement in the reaction progress. The results indicate the mixing frequency being dominated by scales different that that in Eq. 6 for these conditions.

Most future work in calculations of the PPJB ought to be devoted to determining a more suitable scaling for the mixing frequency in LES-PDF calculations, and exploring a framework for the RANS-PDF calculations where C_ϕ does not significantly alter the scalar flux. Future studies ought to focus comparison on the regions of the flow which have been most challenging to model; the fuel consumption index shown in Figure 21 is introduced to provide an efficient way to compare the quality of calculations. This figure, which succinctly summarizes the calculations of the entire flame series, highlights the remaining challenges that lie ahead in understanding these flames.

Since the mixing models are the greatest source of modeling uncertainty in these and previous calculations, further experimental study focused on characterizing the mixing processes in these flames would be insightful. The most direct way to characterize the mixing is to measure the conditional diffusion of chemical species, which then need to be compared to the conditional diffusion obtained from each mixing model. Additionally, measurements of the scalar dissipation rate of chemical species would be useful in a comparison to the scalar dissipation rate implied by each mixing model.

Future calculations ought to seek improvement where the current calculations and previous calculations have shortcomings, that is, in predicting the fuel consumption in PM1-150 and PM1-200 at x/D of 30 and beyond. It is emphasized here that the mixing models play a critical role in determining the reaction progress in these regions. A thorough understanding of the sensitivity of each calculation to all aspects of the mixing models ought to be demonstrated in future studies and compared to the sensitivities observed here. While this work and the previously mentioned studies have all advanced the understanding of these flames and the performance of the models in these conditions, there still remains work to be done in formulating a robust computational framework which performs well in this interesting, challenging, and practical combustion regime.

6. Acknowledgements

This work was supported in part by NSF Award No. CBET-1033246. This research was made with Government support under and awarded by DoD, Air Force Office of Scientific Research, National Defense Science and Engineering Graduate (NDSEG) Fellowship, 32 CFR 168a.

References

[1] U.S. Energy Information Administration, *International Energy Outlook*, Washington D.C., DOE/EIA-0484 (2011).
[2] G. Yu, C.K. Law, and C.K. Wu, *Laminar flame speeds of hydrocarbon+air mixtures with hydrogen addition*, Combust. Flame 63 (1986), pp. 339–347.
[3] S. Correa, *A review of NO_x formation in gas-turbine combustion*, Combust. Sci. Tech. 87 (1992), pp. 327–362.
[4] J.Y. Ren, W. Qin, F.N. Egolfopoulos, and T.T. Tsotsis, *Strain-rate effects on hydrogen-enhanced lean premixed combustion*, Combust. Flame 124 (2001), pp. 717–720.
[5] Y. Huang and V. Yang, *Dynamics and stability of lean-premixed swirl-stabilized combustion*, Prog. Energy Combust. Sci. 35 (2009), pp. 293–364.
[6] T. Lieuwen, H. Torres, C. Johnson, and B.T. Zinn, *A mechanism of combustion instability in lean premixed gas turbine combustors*, J. Eng. Gas Turb. Power 123 (2001), pp. 182–189.
[7] S. Ducruix, T. Schuller, D. Durox, and S. Candel, *Combustion dynamics and instabilities: elementary coupling and driving mechanisms*, J. Propul. Power 19 (2003), pp. 722–734.
[10] M.J. Dunn, A.R. Masri, and R.W. Bilger, *A new piloted premixed jet burner to study strong finite-rate chemistry effects*, Combust. Flame 151 (2007), pp. 46–60.
[10] M.J. Dunn, A.R. Masri, R.W. Bilger, R.S. Barlow, and G.H.Wang, *The compositional structure of highly turbulent piloted premixed flames issuing into a hot coflow*, Proc. Combust. Inst. 32 (2009), pp. 1779–1786.
[10] M.J. Dunn, A.R. Masri, R.W. Bilger, and R.S. Barlow, *Finite-rate chemistry effects in highly sheared turbulent premixed flames*, Flow Turbul. Combust. 1386-6184 (2010), pp. 1–28.
[11] D.H. RowinsHaworth1986ki and S.B. Pope, *PDF calculations of piloted premixed jet flames*, Combust. Theory Model. 15 (2011), pp. 245–266.
[12] H. Wang and S.B. Pope, *Lagrangian investigation of local extinction, re-ignition and auto-ignition in turbulent flames*, Combust. Theory Model. 12 (2008), pp. 857–882.
[13] J. Xu and S.B. Pope, *PDF calculations of turbulent nonpremixed flames with local extinction*, Combust. Flame 123 (2000), pp. 281–307.
[14] R. Cao, S.B. Pope, and A.R. Masri, *Turbulent lifted flames in a vitiated coflow investigated using joint PDF calculations*, Combust. Flame 142 (2005), pp. 438–453.
[15] C. Duwig, K.J. Nogenmyr, C.K. Chan, M.J. Dunn, *Large Eddy Simulations of a piloted lean premix jet flame using finite-rate chemistry*, Combust. Theory Model. 15 (2011), pp. 537–568.
[16] S. Amzin, N. Swaminathan, and J.W. Rogerson, *Conditional moment closure for turbulent premixed flames, 23rd International Colloquium on the Dynamics of Explosions and Reactive Systems*, July 24–29, 2011.
[17] V.N. Prasad, K.H. Luo, and W.P. Jones, *LES-PDF simulation of a highly sheared turbulent piloted premixed flame*, 7th Mediterranean Combustion Symposium, September 11-15, 2011.
[18] Y. Chen and M. Ihme, *Flame Characterization of a Piloted Premixed Jet Burner*, Spring Technical Meeting of the Central States Section of the Combustion Institute, April 22-24, 2012.
[19] S.B. Pope, *PDF methods for turbulent reactive flows*, Prog. Energy Combust. Sci. 11 (1985), pp. 119–192.
[20] S.B. Pope, *Stochastic Lagrangian models for turbulence*, Annual Rev. Fluid Mech. 26 (1994), pp. 23–63.
[21] S.B. Pope, *Turbulent Flows*, Cambridge University Press, Cambridge, 2000.
[22] R.S. Barlow and J.H. Frank, *Effects of turbulence on species mass fractions in methane-air jet flames*, Proc. Combust. Inst. 27 (1998), pp. 1087–1095.
[23] R.P. Lindstedt, S.A. Louloudi, and E.M. Vaos, *Joint scalar probability density function modeling of pollutant formation in piloted turbulent jet diffusion flames with comprehensive chemistry*, Proc. Combust. Inst. 28 (2000), pp. 149–156.
[24] R. Cao, H. Wang, S.B. Pope, S.B., 2007, *The effect of mixing models in PDF calculations of piloted jet flames*, Proc. Combust. Inst. 31 (2007), pp. 1543–1550.
[25] R. Cabra, T. Myhrvold, J.Y. Chen, R.W. Dibble, A.N. Karpetis, and R.W. Barlow, *Simultaneous laser Raman-Rayleigh-LIF measurements and numerical modeling results of a lifted turbulent H_2/N_2 jet flame in a vitiated coflow*, Proc. Combust. Inst. 29 (2002), pp. 1881–1888.
[26] A.R. Masri, R. Cao, S.B. Pope, and G.M. Goldin, *PDF calculations of turbulent lifted flames of H_2/N_2 fuel issuing into a vitiated co-flow*, Combust. Theory Model. 8 (2004), pp. 1–22.
[27] R.L. Gordon, A.R. Masri, S.B. Pope, and G.M. Goldin, *A numerical study of auto-ignition in turbulent lifted flames issuing into a vitiated co-flow*, Combust. Theory Model. 11 (2007), pp. 351–376.
[28] T. Hůlek and R.P. Lindstedt, *Computations of steady-state and transient premixed turbulent flames using PDF methods*, Combust. Flame 104 (1996), pp. 481–504.
[29] R.P. Lindstedt and E.M. Vàos, *Transported PDF modeling of high-Reynolds-number premixed turbulent flames*, Combust. Flame 145 (2006), pp. 495–511.

[30] M. Stollinger and S. Heinz, *Evaluation of scalar mixing and time scale models in PDF simulations of a turbulent premixed flame*, Combust. Flame 157 (2010), pp. 1671–1685.
[31] M. Muradoglu, S.B. Pope, and D.A. Caughey, *The hybrid method for the PDF equations of turbulent reactive flows: consistency conditions and correction algorithms*, J. Comp. Phys. 172 (2001), pp. 841–878.
[32] D.C. Haworth and S.B. Pope, *A generalized Langevin model for turbulent flows*, Phys. Fluids 29 (1986), pp. 387–405.
[33] P.R. Van Slooten, Jayesh, and S.B. Pope, *Advances in PDF modeling for inhomogeneous turbulent flows*, Phys. Fluids 10 (1998), pp. 246–265.
[34] S. Subramaniam and S.B. Pope, *A mixing model for turbulent reactive flows based on Euclidean minimum spanning trees*, Combust. Flame 115 (1998), pp. 487–514.
[35] C.J. Sung, C.K. Law, and J.Y. Chen, *An augmented reduced mechanism for methane oxidation with comprehensive global parametric validation*, Proc. Combust. Inst. 27 (1998), pp. 295–304.
[36] S.B. Pope, *Computationally efficient implementation of combustion chemistry using in situ adaptive tabulation*, Combust. Theory Model. 1 (1997), pp. 41–63.
[37] L. Lu and S.B. Pope, *An improved algorithm for in situ adaptive tabulation*, J. Comp. Phys. 228 (2009), pp. 361–386.
[38] R. McDermott and S.B. Pope, *A particle formulation for treating differential diffusion in filtered density function methods*, J. Comp. Phys. 226 (2007), pp. 947–993.
[39] F.A. Williams, available at `http://maeweb.ucsd.edu/combustion/cermech`.
[40] S. Viswanathan, H. Wang, and S.B. Pope, *Numerical implementation of mixing and molecular transport in LES/PDF studies of turbulent reacting flows*, J. Comp. Phys. 230 (2011), pp. 6916–6957.
[41] J.A. Van Oijen and L.P.H. de Goey, *Modelling of premixed laminar flames using flamelet-generated manifolds*, Combust. Sci. Tech. 161 (2000), pp. 113–137.
[42] J.A. Van Oijen, F.A. Lammers, and L.P.H. de Goey, *Modeling of complex premixed burner systems by using flamelet-generated manifolds*, Combust. Flame 127 (2001), pp. 2124–2134.
[43] H.Wang, X. You, A.V. Joshi, S.G. Davis, A. Laskin, F. Egolfopoulos, and C.K. Law, *USC Mech Version II. High-Temperature Combustion Reaction Model of $H_2/CO/C_1$-C_4 Compounds*, May 2007, available at `http://ignis.usc.edu/USC_Mech_II.htm`.
[44] P.J. Colucci, F.A. Jaberi, P. Givi, and S.B. Pope, *Filtered density function for large eddy simulation of turbulent reacting flows*, Phys. Fluids 10 (1998), pp. 499–515.
[45] V. Raman, H. Pitsch, and R.O. Fox, *Hybrid large-eddy simulation/Lagrangian filtered-density-function approach for simulating turbulent combustion*, Combust. Flame 143 (2005), pp. 56–78.
[46] S. James, J. Zhu, and M.S. Anand, *Large eddy simulations of turbulent flames using the filtered density function model*, Proc. Combust. Inst. 31 (2007), pp. 1737–1745.
[47] W.P. Jones and V.N. Prasad, *LES-PDF simulation of a spark ignited turbulent methane jet*, Proc. Combust. Inst. 33 (2011), pp. 1355–1363.
[48] M.B. Nik, S.L. Yilmaz, P. Givi, M.R.H. Sheikhi, and S.B. Pope, *Simulation of Sandia Flame D using velocity-scalar filtered density function*, AIAA J. 48 (2010), pp. 1513–1522.
[49] H. Wang, M. Juddoo, S.H. Starner, A.R. Masri, and S.B. Pope, *A novel transient turbulent jet flame for studying turbulent combustion*, Proc. Combust. Inst. (2012), (accepted).
[50] Y. Yang, H. Wang, S.B. Pope, and J.H. Chen, *Large-eddy simulation/probability density function modeling of a nonpremixed CO/H_2 temporally evolving jet flame*, Proc. Combust. Inst. (2012), (accepted).
[51] S.B. Pope, *Self-conditioned fields for large-eddy simulations of turbulent flows*, J. Fluid Mech. 652 (2010), pp. 139–169.
[52] H. Wang, P.P. Popov, and S.B. Pope, *Weak second-order splitting schemes for Lagrangian Monte Carlo particle methods for the composition PDF/FDF transport equations*, J. Comp. Phys. 229 (2010), pp. 1852–1878.
[53] H. Wang and S.B. Pope, *Large eddy simulation/probability density function modeling of a turbulent $CH_4/H_2/N_2$ jet flame*, Proc. Combust. Inst. 33 (2011), pp. 1319–1330.
[54] C.D. Pierce and P. Moin, *Progress-variable approach for large-eddy simulation of non-premixed turbulent combustion*, J. Fluid Mech. 504 (2004), pp. 73–97.
[55] A.W. Vreman, *An eddy-viscosity subgrid-scale model for turbulent shear flow: algebraic theory and applications*, Phys. Fluids 16 (2004), pp. 3670–3681.
[56] P.P. Popov, S. Viswanathan, H. Wang, S.B. Pope, 7th US National Technical Meeting of the Combustion Institute, March, 2011, pp. 1C16.

Table 1. Properties of the inflowing streams for the Piloted Premixed Jet Burner.

Stream	Velocity (m/s)	Temperature (K)	Equivalence Ratio	Fuel / Oxidizer	Diameter (mm)
Jet	50-200	300	0.5	Methane / Air	4.0
Pilot	5.3	2280	1.0	Methane / Air	23.5
Coflow	3.7	1500	0.43	Hydrogen / Air	197

Table 2. Model constants for base-case RANS-PDF calculations.

Constant	Value	Usage
C_0	2.1	SLM
C_Ω	0.6893	Definition of the mean frequency Ω
$C_{\omega 1}$	0.70	Turbulence frequency model
$C_{\omega 2}$	0.90	Turbulence frequency model
C_3	1.0	Turbulence frequency model
C_4	0.25	Turbulence frequency model
C_ϕ	1.5	EMST mixing model

Table 3. Thermochemical compositions used for the inlet boundary conditions for each stream. The species are shown in units of mass fraction, and are reported only where the mass fraction exceeds 10^{-6}. Two different boundary condition formulations are shown: compositions taken from chemical equilibrium in the burned streams, and compositions taken from a fully burnt laminar flame in those streams.

Stream	Composition Variable	Equilibrium	Laminar Flame
Jet	O_2	2.26×10^{-1}	2.26×10^{-1}
	CH_4	2.84×10^{-2}	2.84×10^{-2}
	N_2	7.45×10^{-1}	7.45×10^{-1}
	$T(K)$	300	300
Pilot	H_2	3.09×10^{-4}	4.17×10^{-4}
	H	2.11×10^{-5}	3.88×10^{-5}
	O_2	7.72×10^{-3}	1.00×10^{-2}
	OH	2.42×10^{-3}	3.08×10^{-3}
	H_2O	1.20×10^{-1}	1.18×10^{-1}
	CO	1.09×10^{-2}	1.41×10^{-2}
	CO_2	1.34×10^{-1}	1.29×10^{-1}
	N_2	7.25×10^{-1}	7.25×10^{-1}
	T (K)	2280	2240
Coflow	H_2	6.73×10^{-8}	1.02×10^{-6}
	O_2	1.31×10^{-1}	1.32×10^{-1}
	OH	5.24×10^{-5}	1.93×10^{-4}
	H_2O	1.11×10^{-1}	1.11×10^{-1}
	N_2	7.57×10^{-1}	7.57×10^{-1}
	T (K)	1500	1490

Table 4. Test cases for verification of the random walk model for molecular diffusion implementation in the RANS-PDF calculations.

Test Case	Coordinate System	Density	Diffusivity
A	Planar	Uniform	Uniform
B	Cylindrical	Uniform	Uniform
C	Cylindrical	Variable	Uniform
D	Cylindrical	Variable	Variable

Table 5. Grid sizes for LES and LES-PDF calculations. Shown in each column are the grid name, the number of cells in the axial, radial, and angular directions (n_x, n_r, and n_θ), and the total number of cells (n_T), in millions of cells. The next four columns show the errors in the time-averaged mass-weighted resolved mean axial velocity, resolved RMS axial velocity, resolved mean jet mixture fraction, and resolved RMS of the jet mixture fraction for the grid convergence study of the non-reacting flow based on PM1-200. The final six columns show the error in the time-averaged mass-weighted resolved mean jet and pilot mixture fractions, resolved RMS jet and pilot mixture fractions, and the resolved mean and RMS temperature. All errors are evaluated as the maximum difference at x/D of 30 between statistics on the evaluated mesh and the finest mesh examined.

Grid					**NR-200**				**PM1-50**					
Name	n_x	n_r	n_θ	n_T **(MCells)**	$\widetilde{U}$	u_{RMS}	$\widetilde{\xi}_j$	$\widetilde{\xi''_j}$	$\widetilde{\xi}_j$	$\widetilde{\xi''_j}$	$\widetilde{\xi}_p$	$\widetilde{\xi''_p}$	$\widetilde{T}$(K)	$\widetilde{T''}$(K)
G1	96	48	24	0.11	0.104	0.102	0.130	0.041	0.280	0.059	0.121	0.028	298.0	184.4
G2	128	64	32	0.26	0.152	0.031	0.128	0.033	0.036	0.016	0.059	0.026	80.3	37.1
G3	192	96	48	0.88	0.108	0.022	0.082	0.024	0.023	0.017	0.023	0.013	18.4	11.7
G4	256	128	64	2.1	0.044	0.006	0.040	0.011	–	–	–	–	–	–
G5	384	192	96	7.1	–	–	–	–	–	–	–	–	–	–

Table 6. Coefficients in Eq. 8 for the diffusivity of each chemical species, relating the mixture-averaged diffusivity of each species to the temperature, as evaluated from curve-fits evaluated on compositions throughout the entire flamelet manifold.

Species	$\alpha_0(\mathrm{m}^2/\mathrm{s})$	b
H_2	8.00×10^{-5}	1.69
H	12.4×10^{-5}	1.75
O_2	2.03×10^{-5}	1.73
OH	3.22×10^{-5}	1.71
H_2O	2.27×10^{-5}	1.85
HO_2	2.09×10^{-5}	1.72
H_2O_2	2.07×10^{-5}	1.72
CH_3	2.26×10^{-5}	1.73
CH_4	2.30×10^{-5}	1.71
CO	2.08×10^{-5}	1.71
CO_2	1.58×10^{-5}	1.75
CH_2O	1.56×10^{-5}	1.80
C_2H_2	1.67×10^{-5}	1.74
C_2H_4	1.61×10^{-5}	1.76
C_2H_6	1.48×10^{-5}	1.75
N_2	2.17×10^{-5}	1.70

Table 7. Table of computational cost for several different modeling approaches for flame PM1-50. The number of variables used to describe the thermochemistry and the number of unique diffusivities are both indicated before the name of each respective model. The molecular diffusion models are (RW) the random walk in position space (Eq. 1), and (MT) full molecular transport with interaction-by-exchange-with-the-mean mixing and mean drift (Eq. 5).

Methodology	**Chemistry Model**	**Molecular Diffusion**	**CPU Hours**
RANS-PDF	3-FGM	–	1,700
	17-ISAT	–	2,300
	17-ISAT	1-RW	2,400
	54-ISAT	–	3,800
LES-PDF	3-FGM	1-MT	18,000
	17-ISAT	1-MT	52,000
	17-ISAT	17-MT	190,000

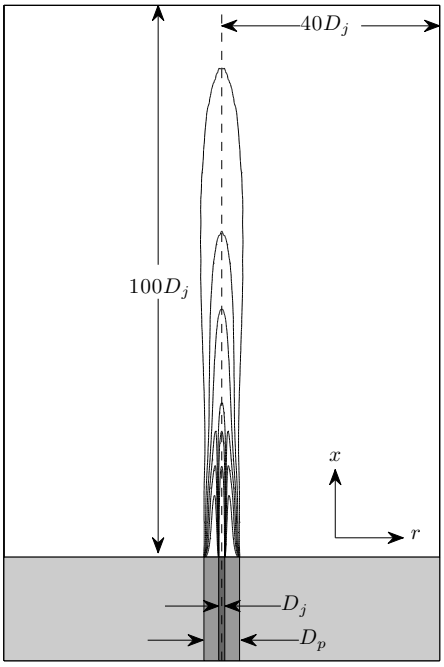

Figure 1. Sketch of computational domain for RANS-PDF calculations. The centerline is indicated by the vertical dotted line, and the domain extends to the boundary of the white colored region. The extent of the domain in the axial and radial directions is indicated by the vertical and horizontal measurements in the white region, respectively. In the gray region at the bottom, the location of the three stream boundary conditions are shown by shades of gray; outward from the centerline, they are the central jet, the pilot, and the coflow. The dimensions at the bottom are of the diameters of the jet and pilot. A contour of the mean CO_2 mass fraction from a calculation of PM1-100 is shown in the sketch of the computational domain.

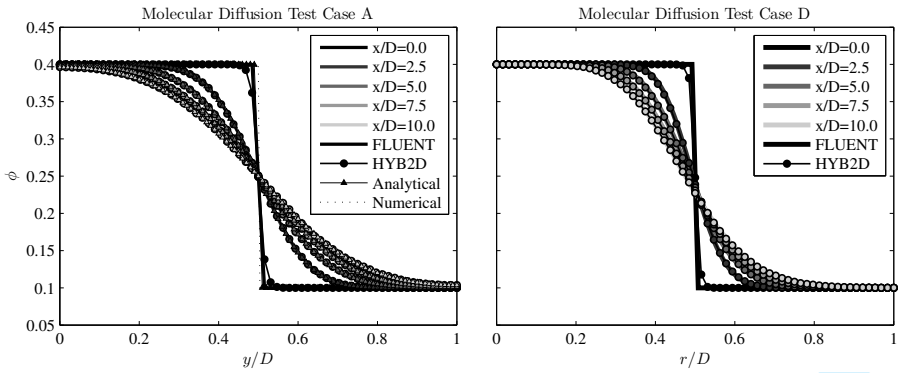

Figure 2. Mass-weighted mean species mass fractions in tests of the molecular diffusion implementation. The figure on the left shows the results from the constant-density, constant-diffusivity test case in Cartesian coordinates; the figure on the right shows the results from the variable-density, variable-diffusivity test case in cylindrical coordinates. The color of the lines denotes the axial location as indicated in the legend. The solid lines are from a verification of the test case using the commercial code Fluent; the lines with circle markers are from the new molecular diffusion implementation in the RANS-PDF code, HYB2D; the lines with triangular markers are from an analytical solution; the dashed lines are from a numerical finite difference solution.

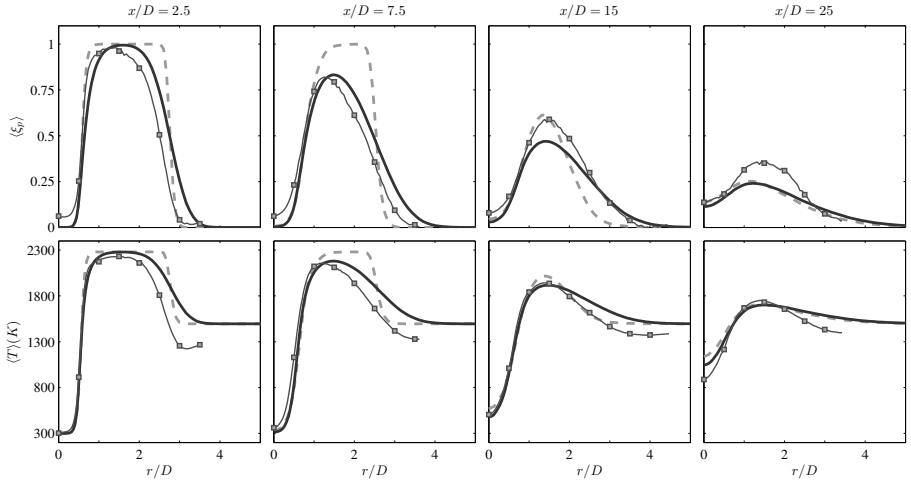

Figure 3. Radial profiles of mass-weighted mean pilot mass fraction (top plots) and mass-weighted mean temperature (bottom plots) from calculations and measurements of flame PM1-50 showing the effect of modeling molecular diffusion. The axial location is indicated at the top of each column, and increases from left to right. Dashed gray line – RANS-PDF without molecular diffusion; Solid line – RANS-PDF with molecular diffusion; Lines with squares: experimental data [10].

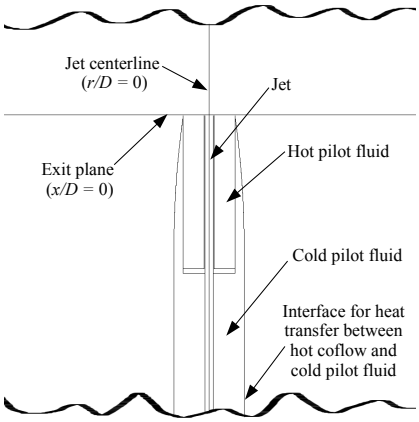

Figure 4. Sketch showing the geometry used to formulate inflow boundary conditions with heat transfer from the coflow to the cold pilot fluid. The upstream region extends below the jet centerline, and the downstream region extends above the jet centerline. In the adiabatic calculations, there is no heat transfer at the pilot-coflow interface, but in the non-adabatic calculations, heat transfer occurs between the hot coflow and cold pilot fluid.

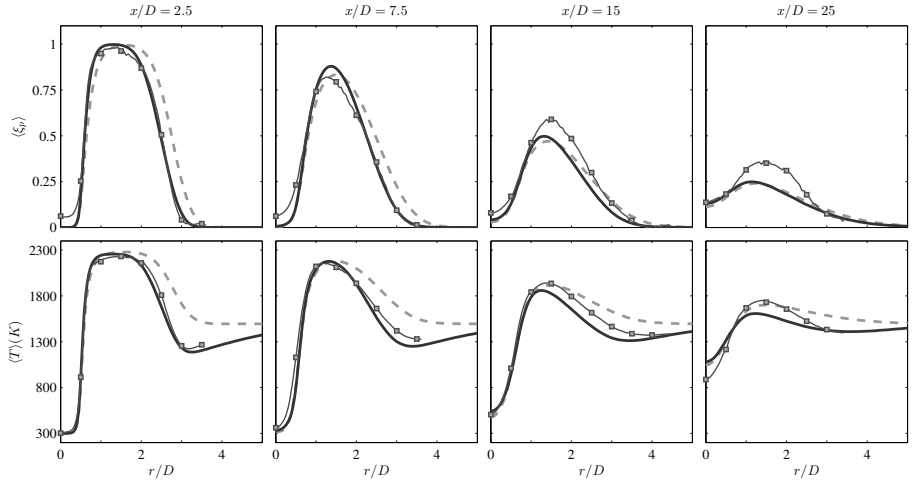

Figure 5. Radial profiles of time-averaged mass-weighted mean pilot mass fraction (top plots) and time-averaged mass-weighted mean temperature (bottom plots) from calculations and measurements of flame PM1-50 showing the effect of modeling conjugate heat transfer between the pilot and coflow. The axial location is indicated at the top of each column. Dashed gray line: RANS-PDF calculations with adiabatic boundary conditions; Solid line: RANS-PDF calculations with conjugate heat transfer; Lines with squares: experimental data [10].

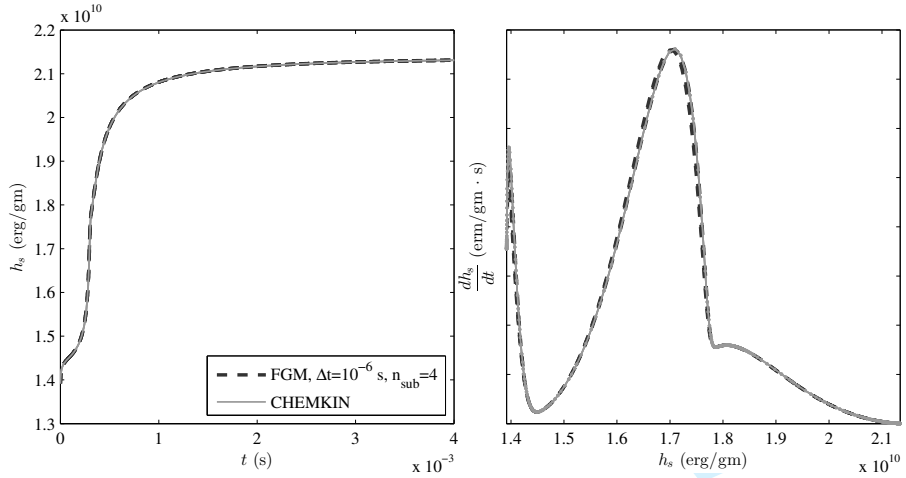

Figure 6. Plots of sensible enthalpy, h_s, versus time, t, (left) and the time rate of change of sensible enthalpy, $\dot{h}_s$ or dh_s/dt, versus sensible enthalpy (right) for jet and pilot mixture fractions of (0.47, 0.50). The dark dashed line is computed using a FGM using a time step, Δt, of 10^{-6} and 4 time sub-steps; the light solid line is computed using the commercial software Chemkin using appropriately low values for error tolerances. The rapid variation at the initial time step is due to the reaction of radicals from the pilot and coflow mixtures.

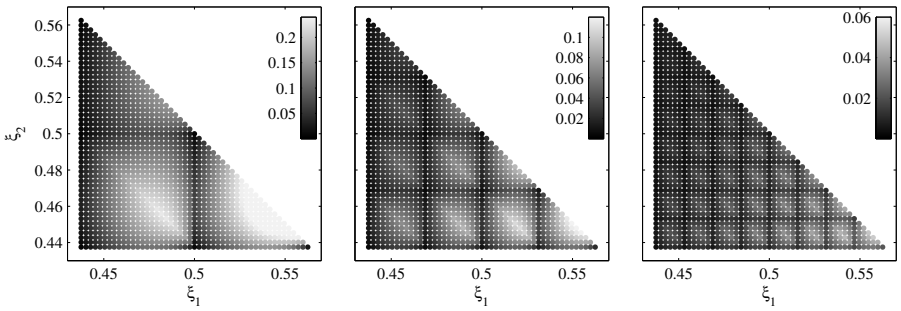

Figure 7. Plot in the two-dimensional mixture fraction space colored by the error in ignition delay time as defined in Eq. 4 for FGM's constructed on three different grids. The grids are, from left to right, FGM-16, FGM-32, and FGM-64. The color scaling varies for each plot and is indicated by the colorbar in the upper right corner of each plot.

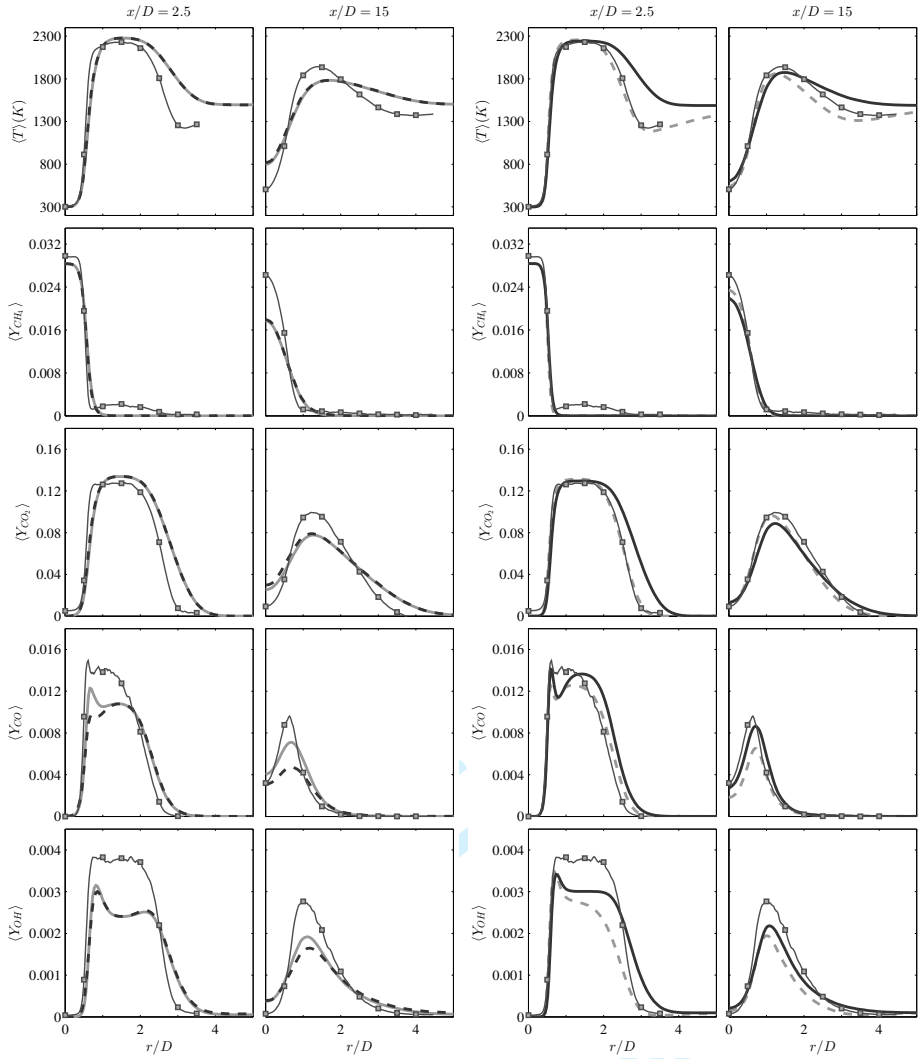

Figure 8. Radial profiles of (from top to bottom) time-averaged mass-weighted mean temperature, and time-averaged mass-weighted mean mass fractions of species CH_4, CO_2, CO, and OH in the RANS-PDF calculations of PM1-50 using different chemistry models and boundary conditions. Left-most two columns: equilibrium boundary conditions and chemistry modeled with: detailed chemistry using ARM-1 and ISAT (dark dashed lines) and FGM-AI (light solid line); Right-most two columns: laminar flame boundary conditions using: ARM-1 and ISAT (light dashed line) and FGM-LF (dark solid line); Lines with squares: experimental data [10].

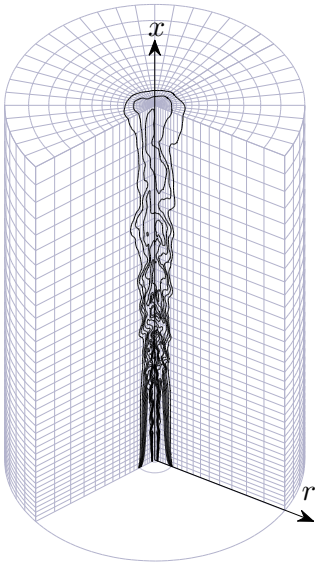

Figure 9. Computational domain for the LES-PDF calculations. The axial and radial directions are indicated by the arrows, and the vertical arrow coincides with the centerline of the jet. Only one fifth of the grid points from grid G3 are shown in each axial and radial direction. The cutaway in the $x - r$ plane shows a contour of the instantaneous resolved CO_2 mass fraction from a calculation of PM1-100. In the plane at the bottom of the cutaway, the diameter of the pilot and jet are shown.

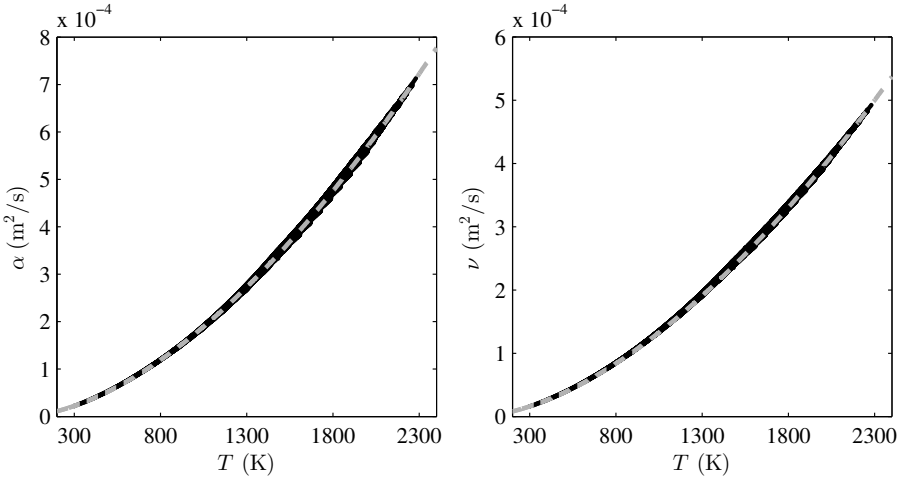

Figure 10. Molecular transport properties as prescribed in LES-PDF calculations as functions of temperature. The thermal diffusivity is shown in the left plot, and the kinematic viscosity is shown in the right plot. In both plots, the black dots indicate the transport properties as evaluated on the FGM, and the gray dashed lines indicate the curve-fits used to Eqs. 2 and 7 that are prescribed in the LES-PDF calculations.

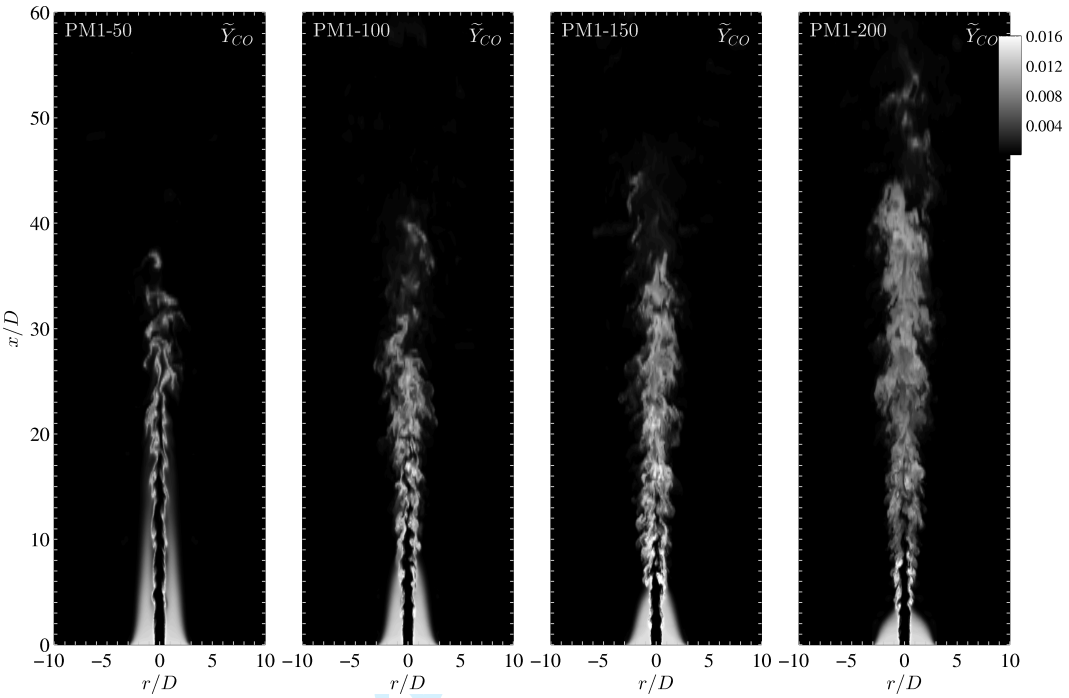

Figure 11. Contour plots of instantaneous fields of resolved CO mass fraction from LES-PDF calculations of all four PPJB flames on grid G4 using the mechanism ARM-1 to describe the chemistry.

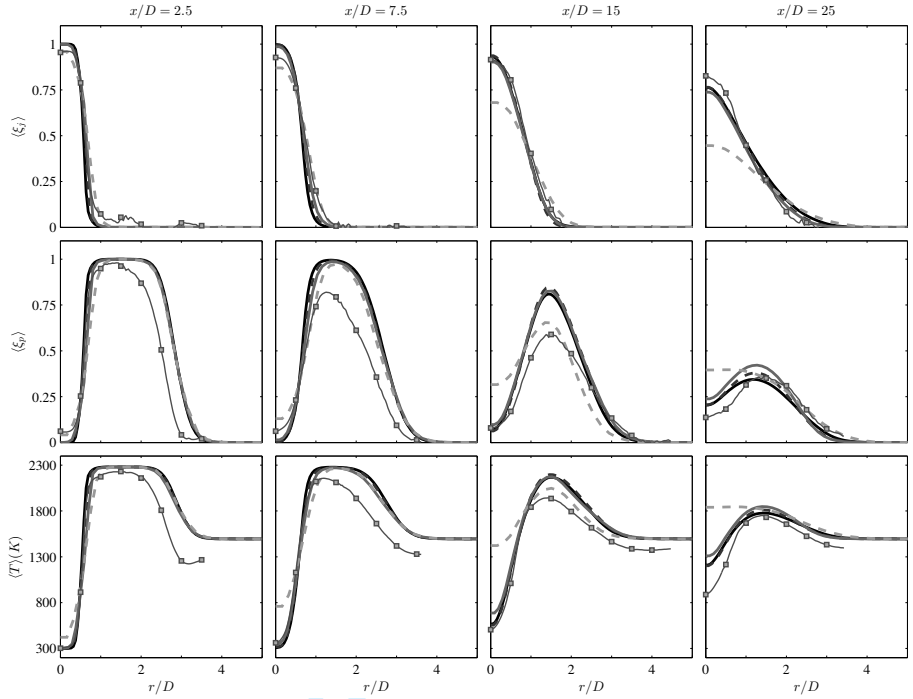

(a)

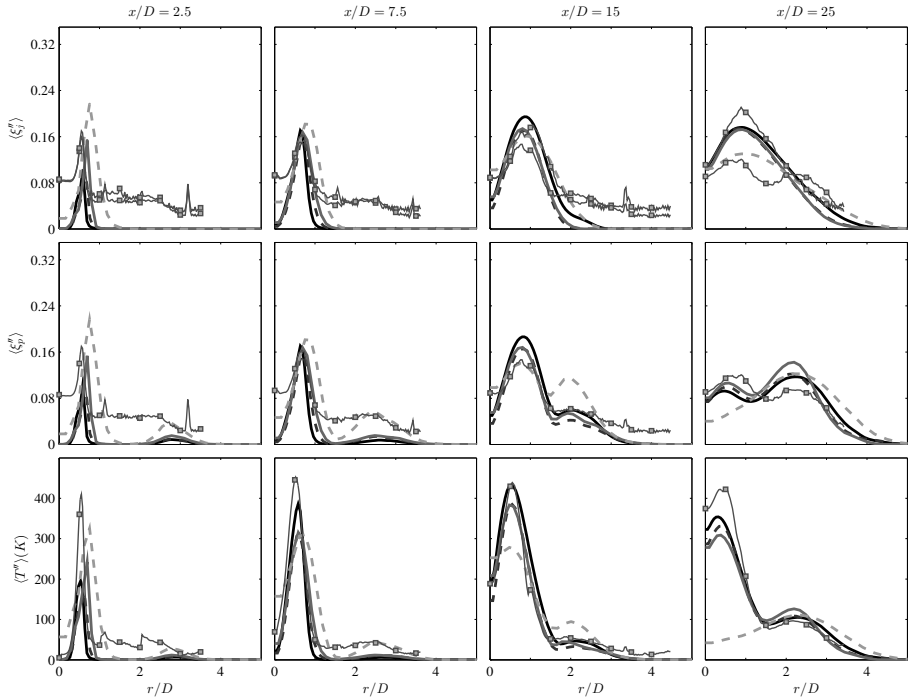

(b)

Figure 12. Radial profiles of the time-averaged mass-weighted resolved mean (a) and RMS of the resolved scalar (b) for the jet mixture fraction (top row), pilot mixture fraction (middle row), and temperature (bottom row) in the convergence study of the LES-PDF calculations of flame PM1-50. The axial location is indicated at the top of each column. Dashed light gray: G1; Solid gray: G2; Dashed dark gray: G3; Solid black: G4; Lines with squares: experimental data [10].

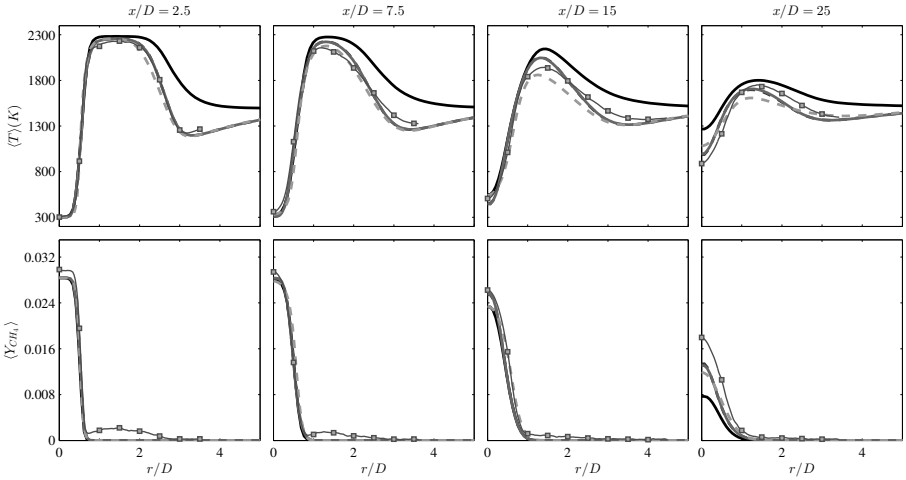

(a)

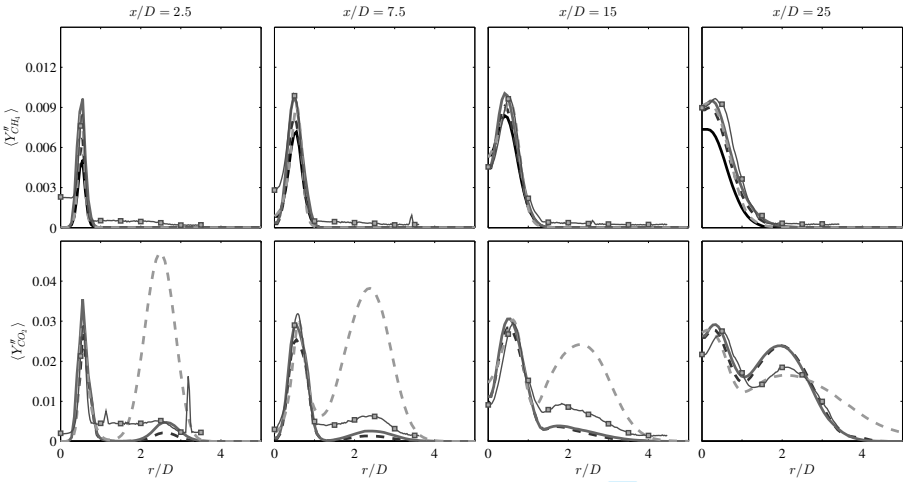

(b)

Figure 13. Radial profiles of the time-averaged mass-weighted resolved mean (a) and RMS statistics in the base case LES-PDF and RANS-PDF calculations of flame PM1-50. Dark solid line: LES-PDF without heat loss; Gray solid line: LES-PDF with heat loss (total RMS); Gray dashed line: LES-PDF with heat loss (RMS of resolved scalar); Light gray dashed line: base case RANS-PDF; Lines with squares: experimental data [10].

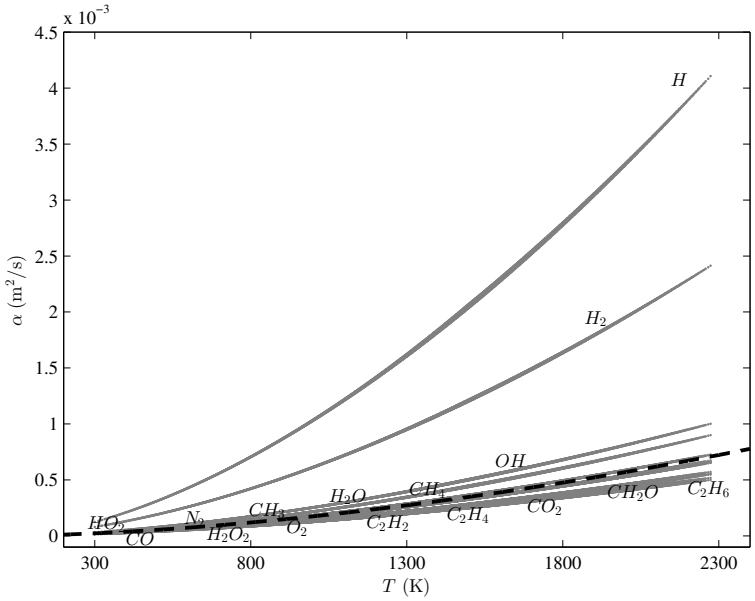

Figure 14. Molecular diffusivity of the chemical species in the ARM-1 mechanism as evaluated from compositions on the FGM and plotted as functions of temperature. The curve-fit to Eq. 2 for the thermal diffusivity is shown by the black dotted line.

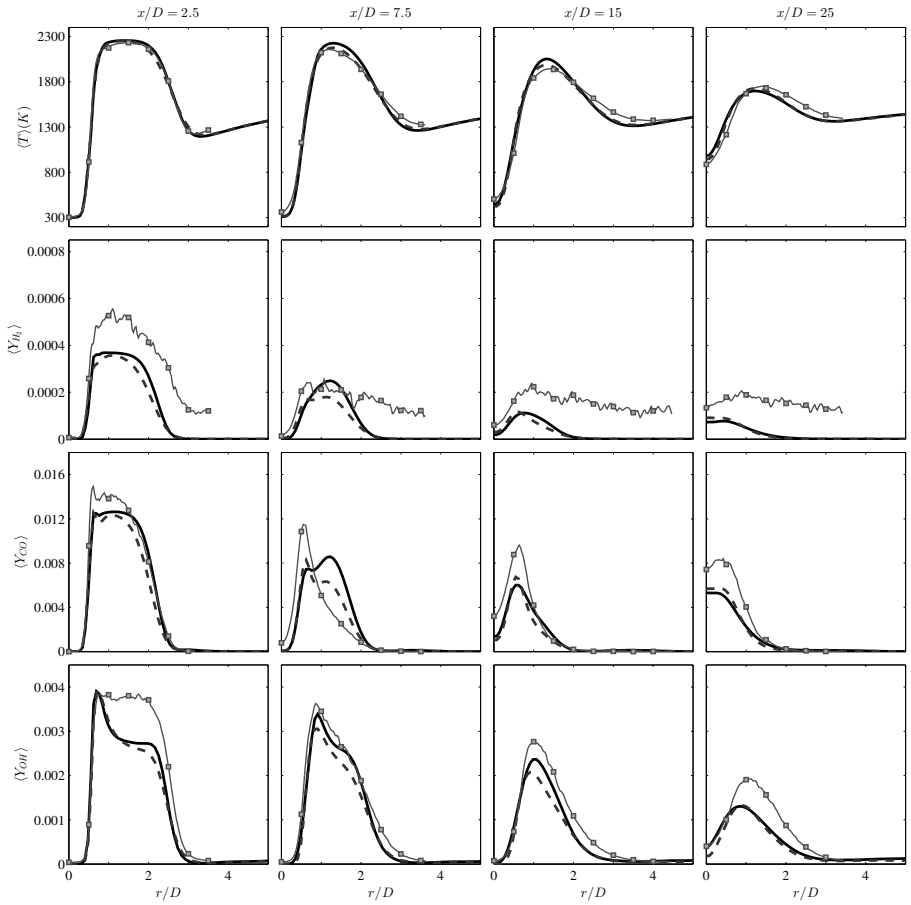

Figure 15. Radial profiles of time-averaged mass-weighted resolved scalars in calculations of PM1-50 with and without differential diffusion. The first row shows the temperature, the next three rows show the mass fraction of the species H_2, CO, and OH. Solid dark line: Without differential diffusion; Dashed gray line: with differential diffusion; Lines with squares: experimental data [10].

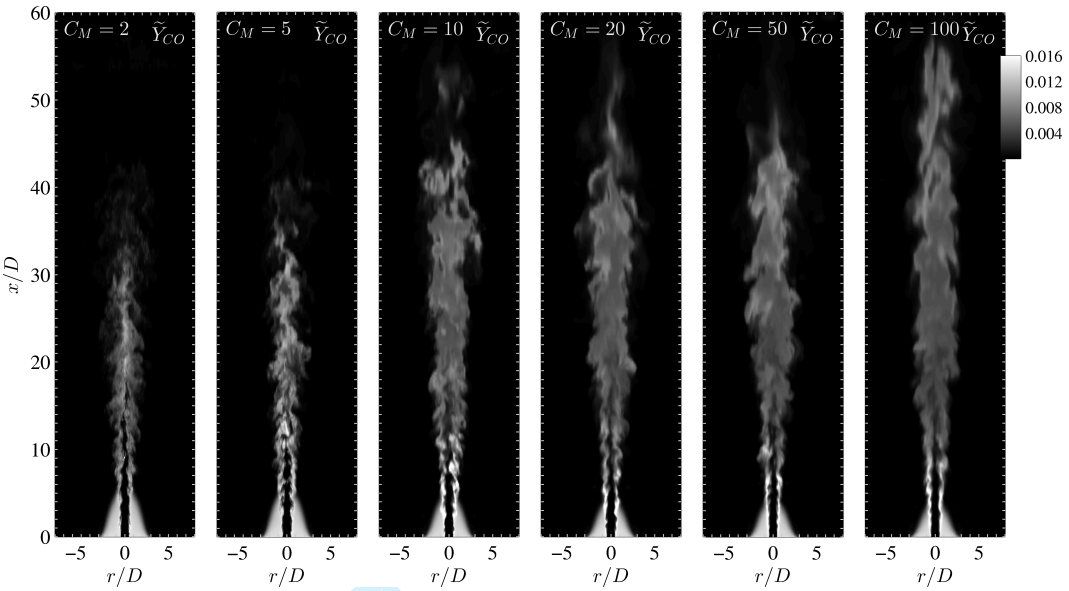

Figure 16. Contour plots of instantaneous resolved mass fraction of CO in the parametric study of C_M for flame PM1-150. The value of C_M used in each calculation increases from 2 to 100 going from left to right, and is indicated in the top left corner of each plot. The value of the resolved CO mass fraction is indicated by the colorbar in the top right corner.

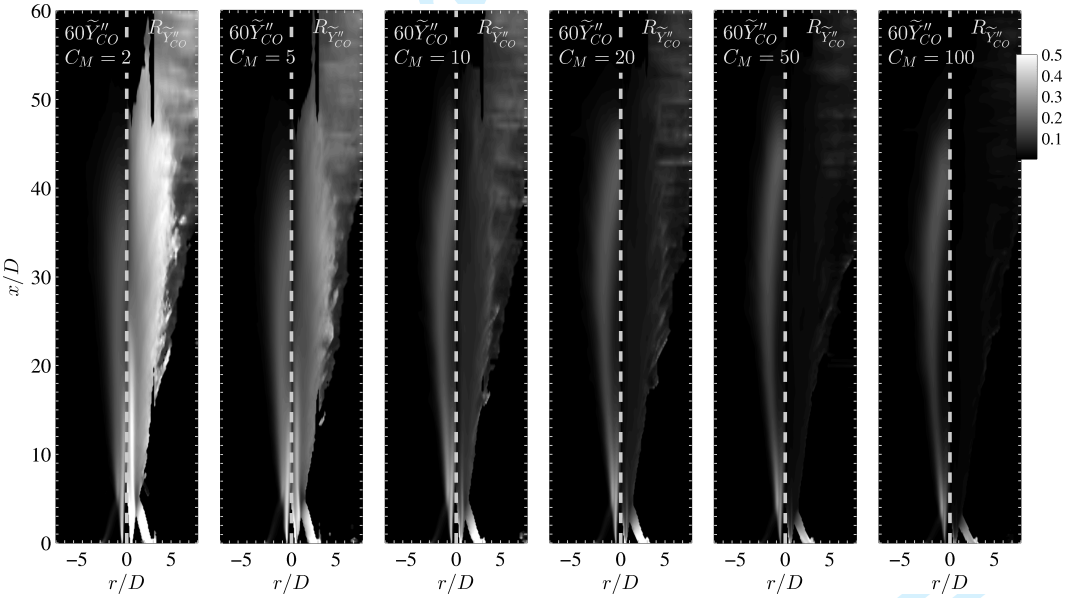

Figure 17. Contour plots of time-averaged mass-weighted total RMS of CO mass fraction (left side) and portion of the total RMS which is residual, $R_{\widetilde{Y}''_{CO}}$, (right side) in the parametric study of C_M for flame PM1-150. The quantity $R_{\widetilde{Y}''_{CO}}$ is defined as the time-averaged mass-weighted residual RMS mass fraction of CO divided by the time-averaged mass-weighted total RMS mass fraction of CO. The magnitude of the total RMS (left side) is multiplied by a factor of 60 so one colorbar is used to show the magnitude of both quantities.

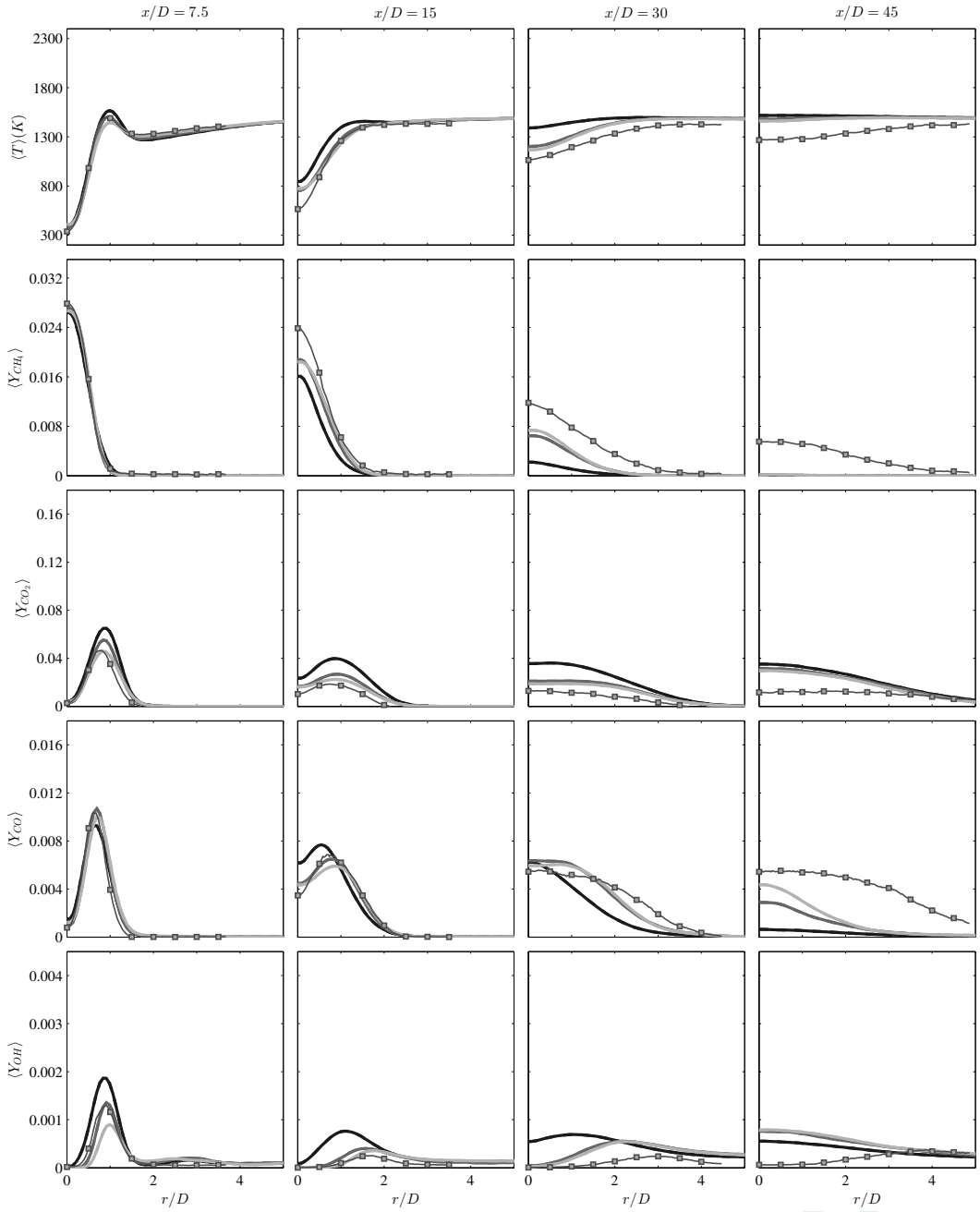

Figure 18. Radial profiles of time-averaged mass-weighted mean resolved scalars in the parametric study of C_M in flame PM1-150. The plotted scalars are, from top row to bottom row, temperature and mass fractions of the species CH_4, CO_2, CO, and OH. Black line: $C_M = 5$; Dark gray line: $C_M = 20$; Light gray line: $C_M = 50$; Lines with squares: experimental data [10].

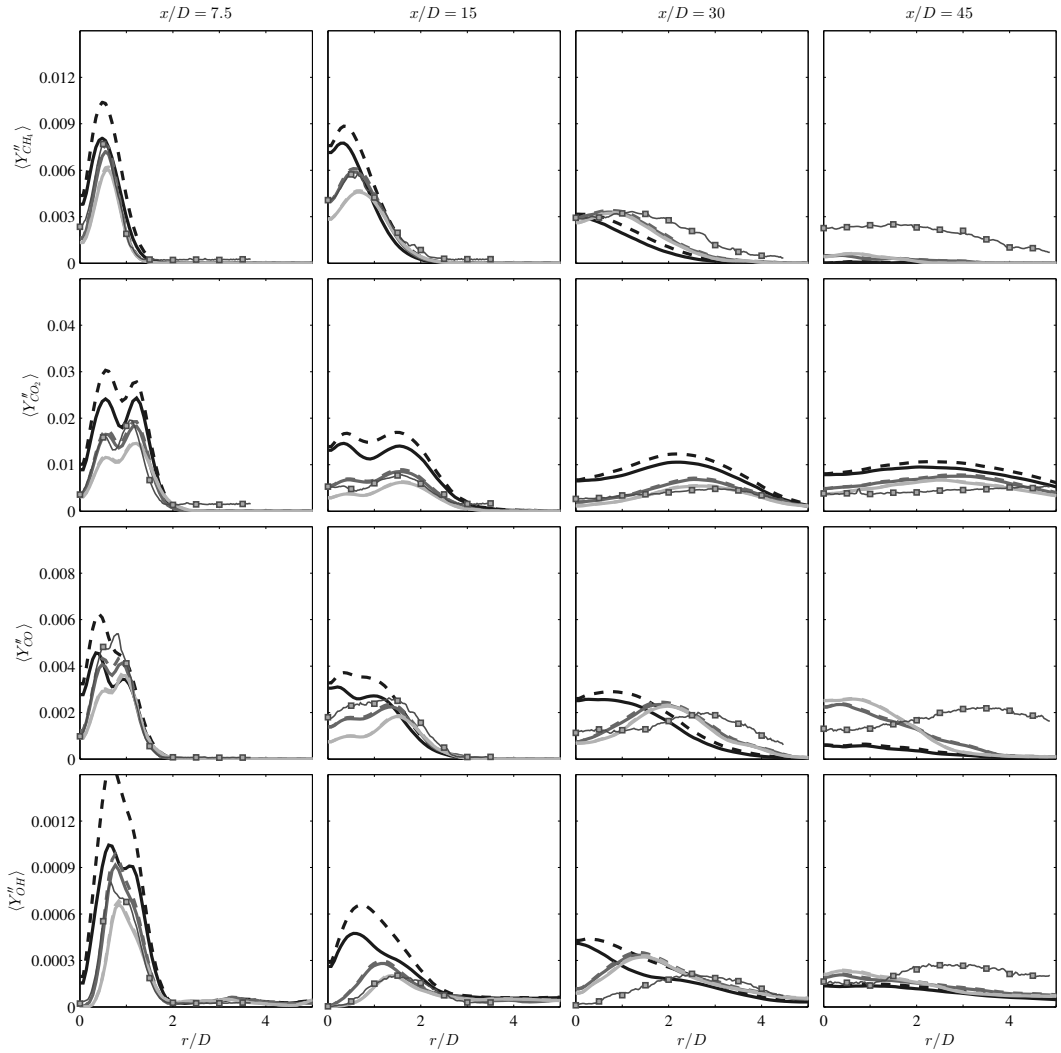

Figure 19. Radial profiles of time-averaged mass-weighted RMS of resolved scalars and total RMS (RMS of resolved fields and residual RMS) in the parametric study of C_M in flame PM1-150. The plotted scalars are, from top row to bottom row, temperature and mass fractions of the species CH_4, CO_2, CO, and OH. Black line: $C_M = 5$; Dark gray line: $C_M = 20$; Light gray line: $C_M = 50$; Solid lines: RMS of resolved scalars; Dashed lines: total RMS; Lines with squares: experimental data [10].

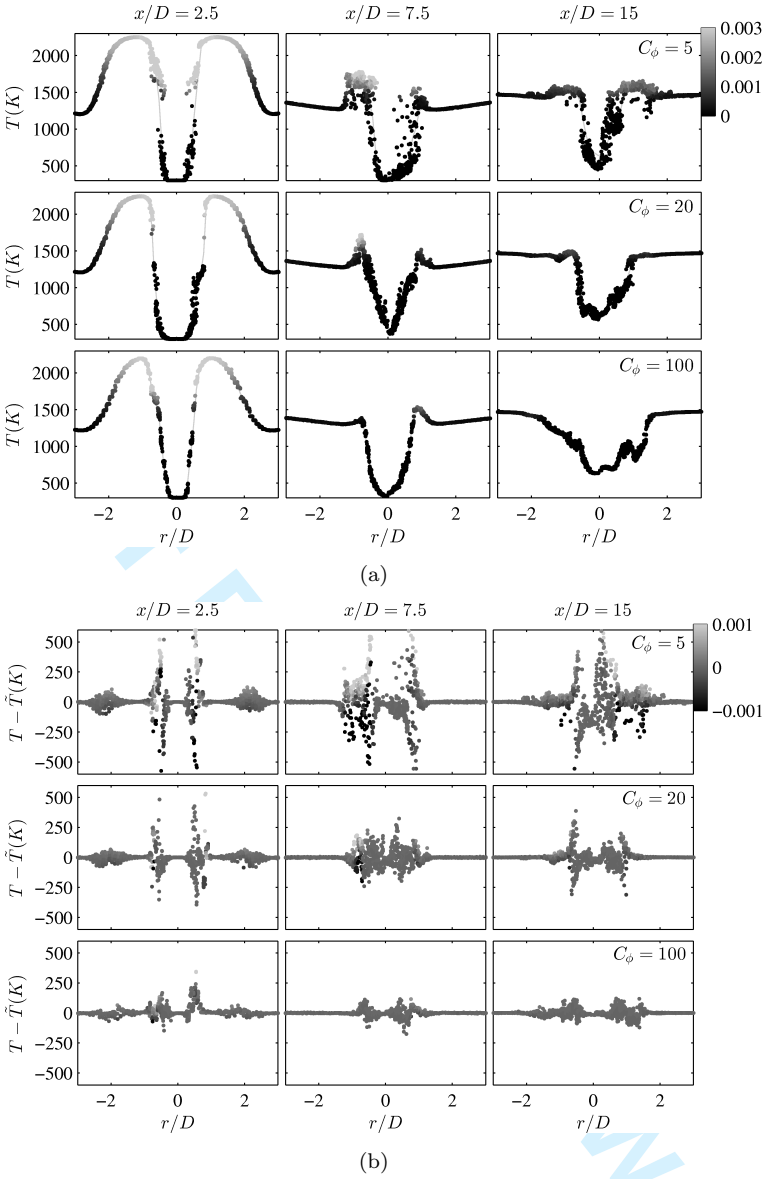

Figure 20. Radial profiles of instantaneous particle quantities from the parametric study of C_M from flame PM1-150. The topmost three rows (a) show the temperature of the particles as a function of the radial position for one row of cells in the calculations. The bottommost three rows (b) show the temperature deviation from the cell mean temperature for the same particles in the same one row of cells. For each set of three columns, the axial location of the plots increase from left to right as indicated above each column. Each row shows results from calculations using a different value of C_M, increase from top row to bottom row as C_M of 5 (top row), C_M of 20 (middle row), and C_M of 100 (bottom row). The particles in the topmost three rows (a) are colored by the particle CO mass fraction, and the particles in the bottommost three rows (b) are colored by the deviation of the CO mass fraction from the cell mean CO mass fraction. The light solid line in the topmost three rows (a) indicates the cell mean temperature for the row of cells plotted.

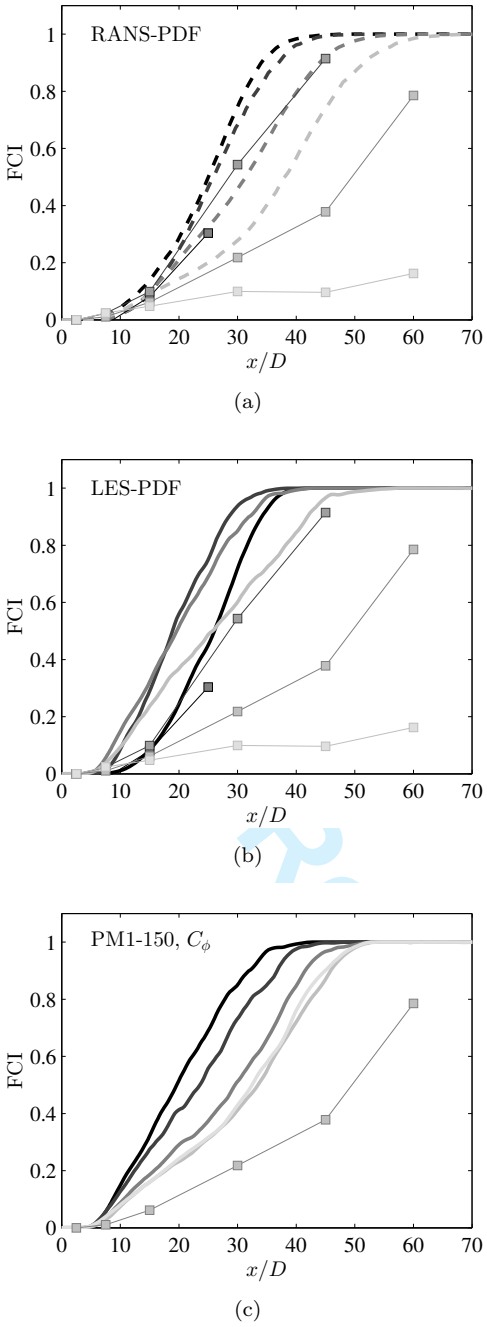

Figure 21. Fuel Consumption Index (FCI) on the centerline of the jet ($r/D = 0$) as a function of axial position (x/D) from the experimental measurements of the PPJB flames and various calculations from this study. In all plots, the experimental measurements are denoted by the lines with square markers. The leftmost plot (a) shows the results from the RANS-PDF calculations in the dashed lines. The rightmost plot (b) shows the results from the LES-PDF calculations in the solid lines. In both (a) and (b), the color of the line denotes the flame. The darkest line is for PM1-50, the second darkest is for PM1-100, the second lightest is for PM1-150, and the lightest is for PM1-200. In the rightmost plot (c), the results from the parameter study of C_M in the LES-PDF calculations of PM1-150 are shown. The line colors, from dark to light, denote values of C_M of 5, 10, 20, 50, and 100.

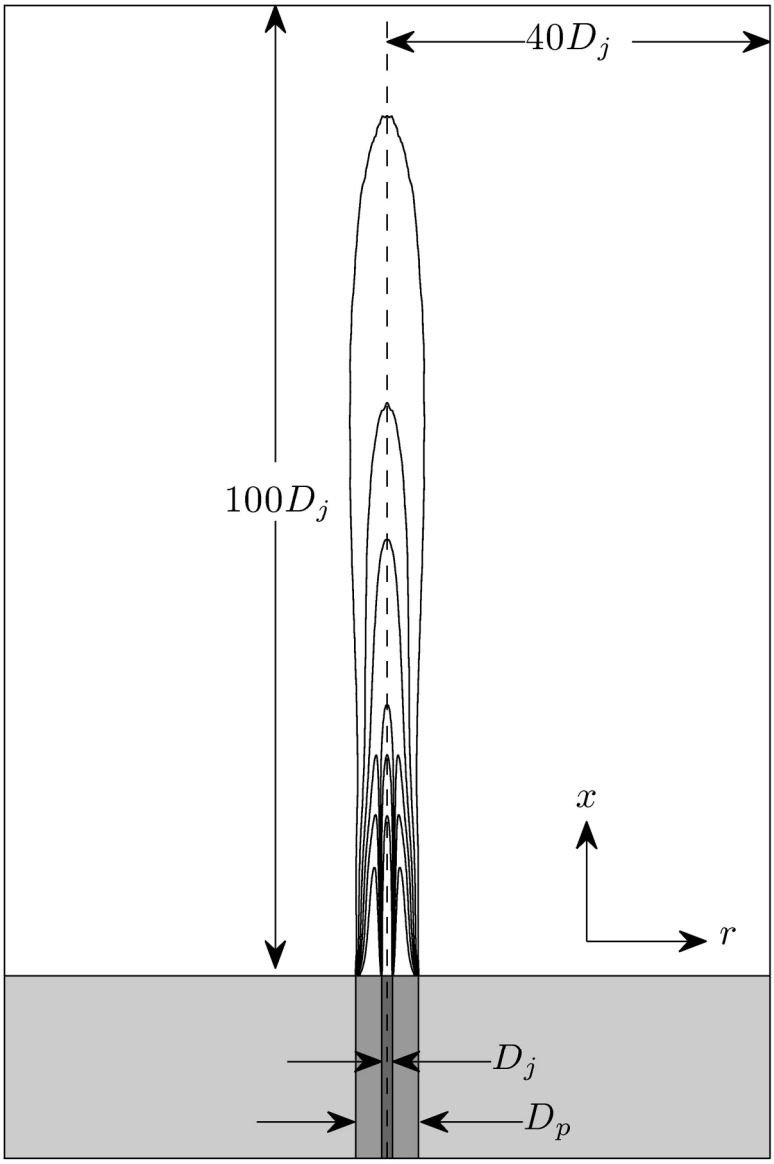

Sketch of computational domain for RANS-PDF calculations. The centerline is indicated by the vertical dotted line, and the domain extends to the boundary of the white colored region. The extent of the domain in the axial and radial directions is indicated by the vertical and horizontal measurements in the white region, respectively. In the gray region at the bottom, the location of the three stream boundary conditions are shown by shades of gray; outward from the centerline, they are the central jet, the pilot, and the coflow. The dimensions at the bottom are of the diameters of the jet and pilot. A contour of the mean CO_2 mass fraction from a calculation of PM1-100 is shown in the sketch of the computational domain.
158x238mm (300 x 300 DPI)

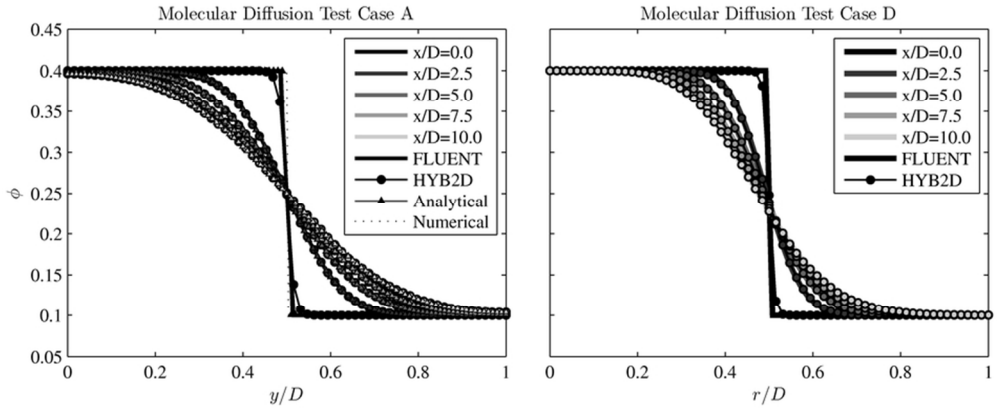

Mass-weighted mean species mass fractions in tests of the molecular diffusion implementation. The figure on the left shows the results from the constant-density, constant-diffusivity test case in Cartesian coordinates; the figure on the right shows the results from the variable-density, variable-diffusivity test case in cylindrical coordinates. The color of the lines denotes the axial location as indicated in the legend. The solid lines are from a verification of the test case using the commercial code Fluent; the lines with circle markers are from the new molecular diffusion implementation in the RANS-PDF code, HYB2D; the lines with triangular markers are from an analytical solution; the dashed lines are from a numerical finite difference solution.
80x33mm (300 x 300 DPI)

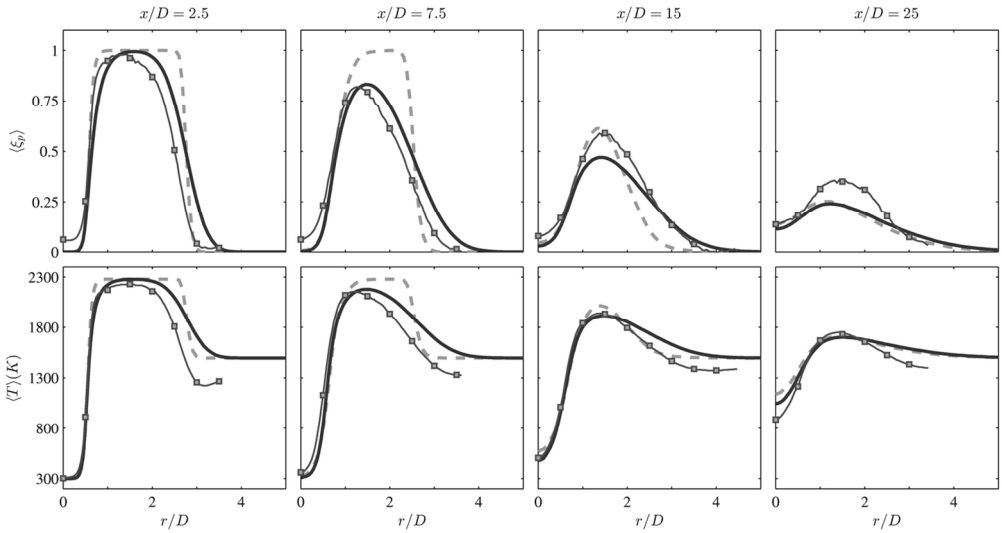

Radial profiles of mass-weighted mean pilot mass fraction (top plots) and mass-weighted mean temperature (bottom plots) from calculations and measurements of flame PM1-50 showing the effect of modeling molecular diffusion. The axial location is indicated at the top of each column, and increases from left to right. Dashed gray line -- RANS-PDF without molecular diffusion; Solid line -- RANS-PDF with molecular diffusion; Lines with squares: experimental data.
124x66mm (300 x 300 DPI)

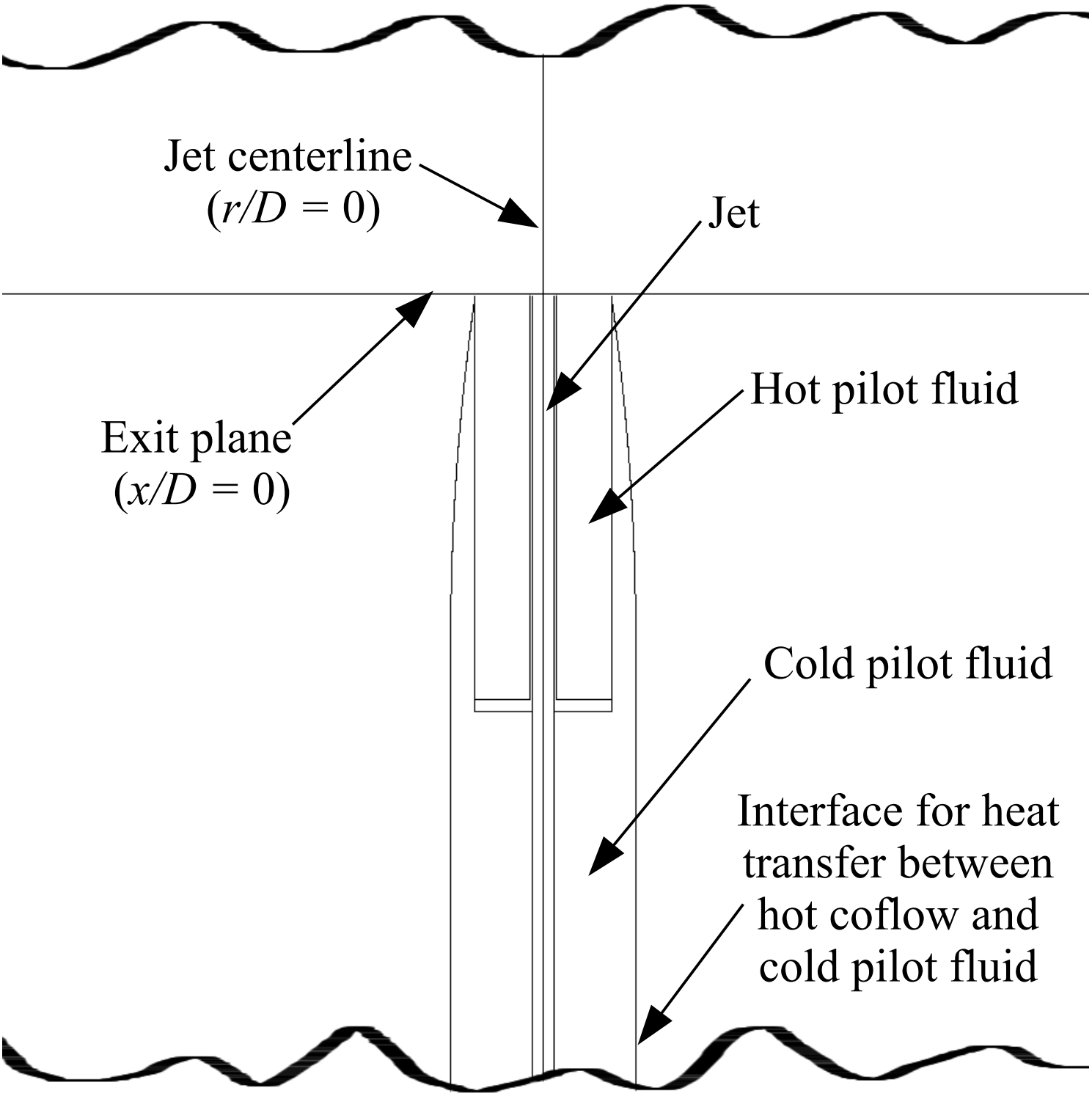
Jet centerline
($r/D = 0$)
Jet
Exit plane
($x/D = 0$)
Hot pilot fluid
Cold pilot fluid
Interface for heat transfer between hot coflow and cold pilot fluid

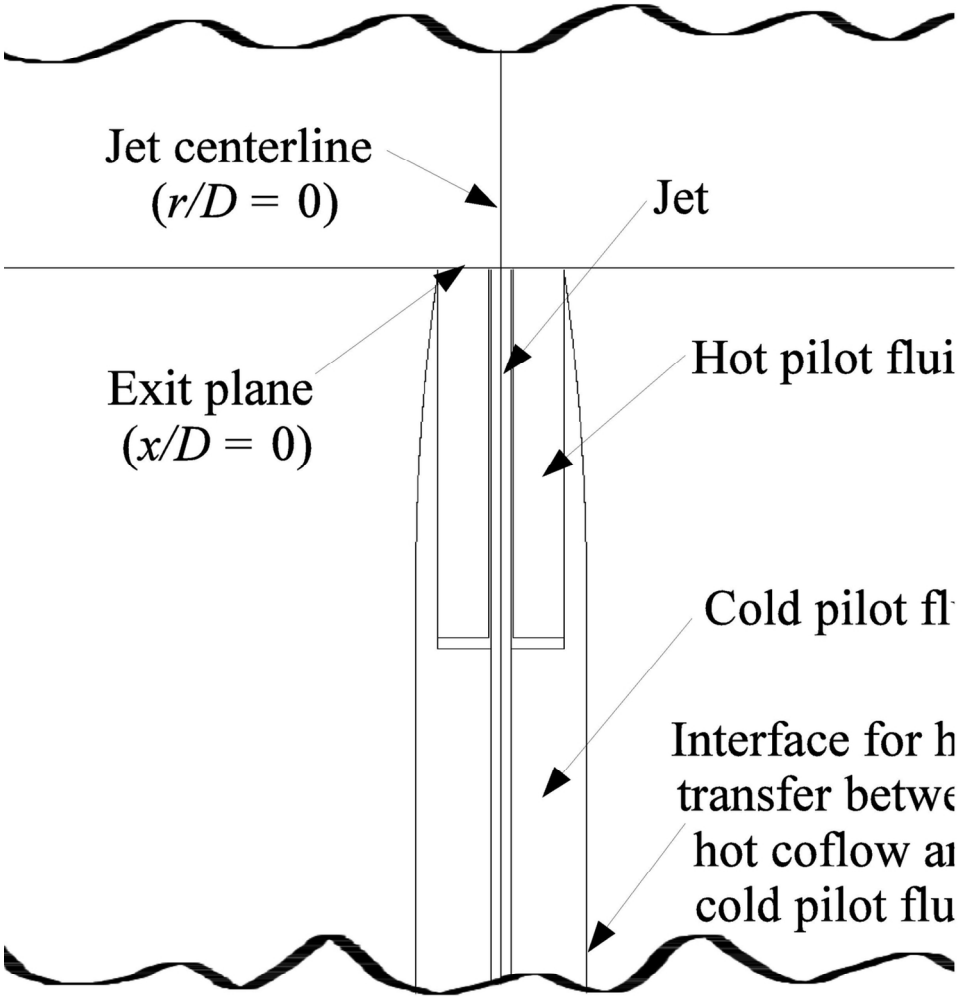

Sketch showing the geometry used to formulate inflow boundary conditions with heat transfer from the coflow to the cold pilot fluid. The upstream region extends below the jet centerline, and the downstream region extends above the jet centerline. In the adiabatic calculations, there is no heat transfer at the pilot-coflow interface, but in the non-adabatic calculations, heat transfer occurs between the hot coflow and cold pilot fluid.
120x134mm (300 x 300 DPI)

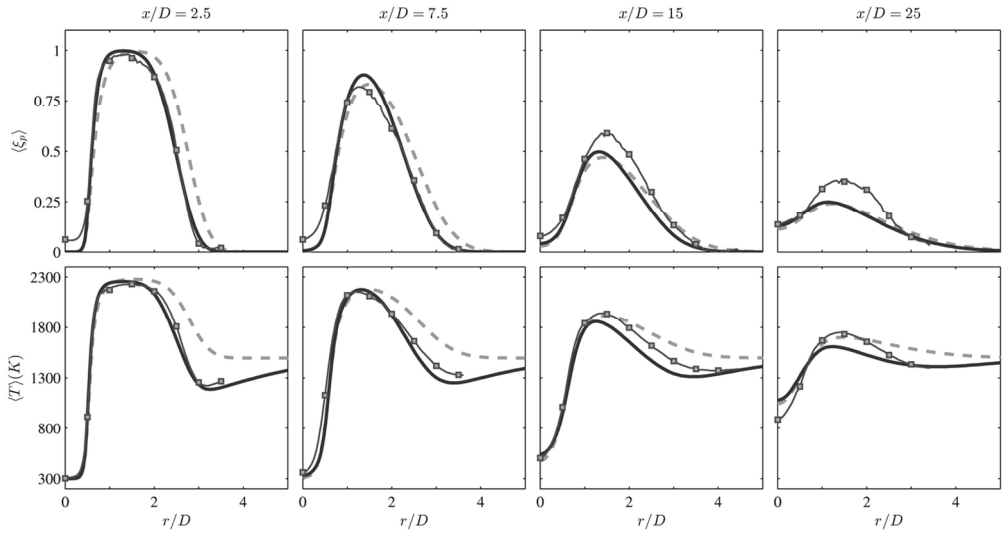

Radial profiles of time-averaged mass-weighted mean pilot mass fraction (top plots) and time-averaged mass-weighted mean temperature (bottom plots) from calculations and measurements of flame PM1-50 showing the effect of modeling conjugate heat transfer between the pilot and coflow. The axial location is indicated at the top of each column. Dashed gray line: RANS-PDF calculations with adiabatic boundary conditions; Solid line: RANS-PDF calculations with conjugate heat transfer; Lines with squares: experimental data.
124x66mm (300 x 300 DPI)

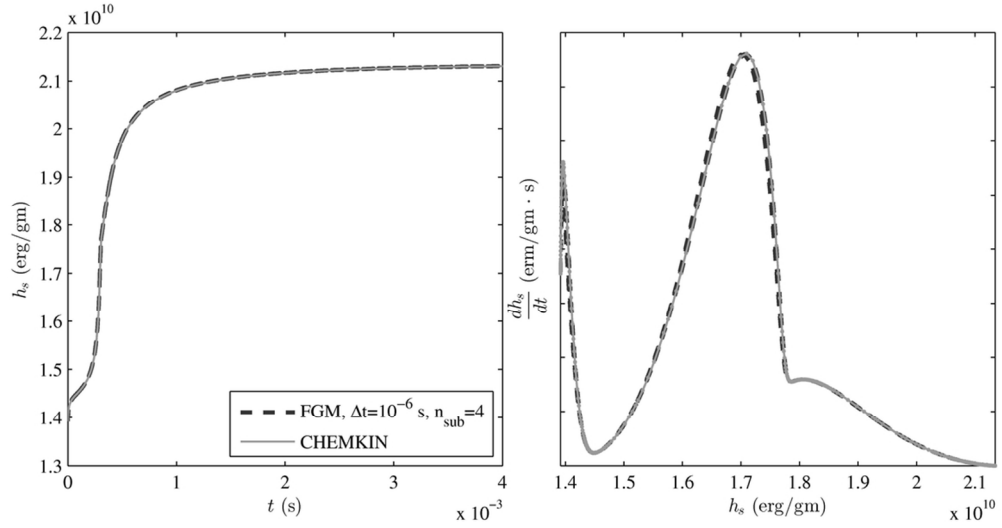

Plots of sensible enthalpy, h_s, versus time, t, (left) and the time rate of change of sensible enthalpy, dh_s/dt, versus sensible enthalpy (right) for jet and pilot mixture fractions of (0.47, 0.50). The dark dashed line is computed using a FGM using a time step, of 10^{-6} and 4 time sub-steps; the light solid line is computed using the commercial software Chemkin using appropriately low values for error tolerances. The rapid variation at the initial time step is due to the reaction of radicals from the pilot and coflow mixtures.
98x51mm (300 x 300 DPI)

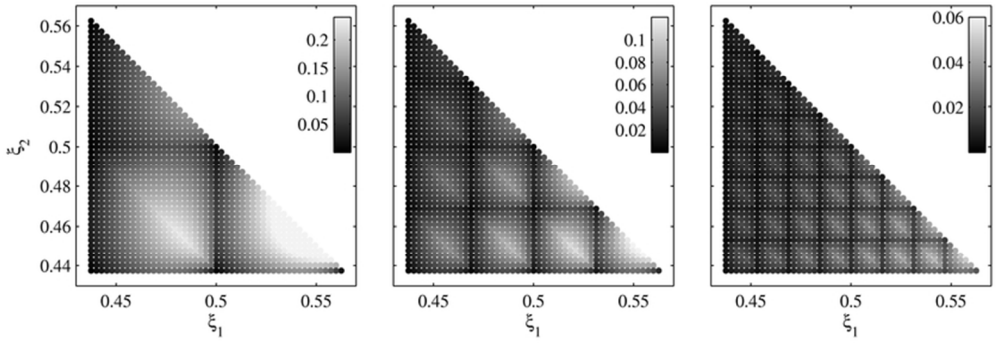

Plot in the two-dimensional mixture fraction space colored by the error in ignition delay time as defined in Eq. 4 for FGM's constructed on three different grids. The grids are, from left to right, FGM-16, FGM-32, and FGM-64. The color scaling varies for each plot and is indicated by the colorbar in the upper right corner of each plot.
71x25mm (300 x 300 DPI)

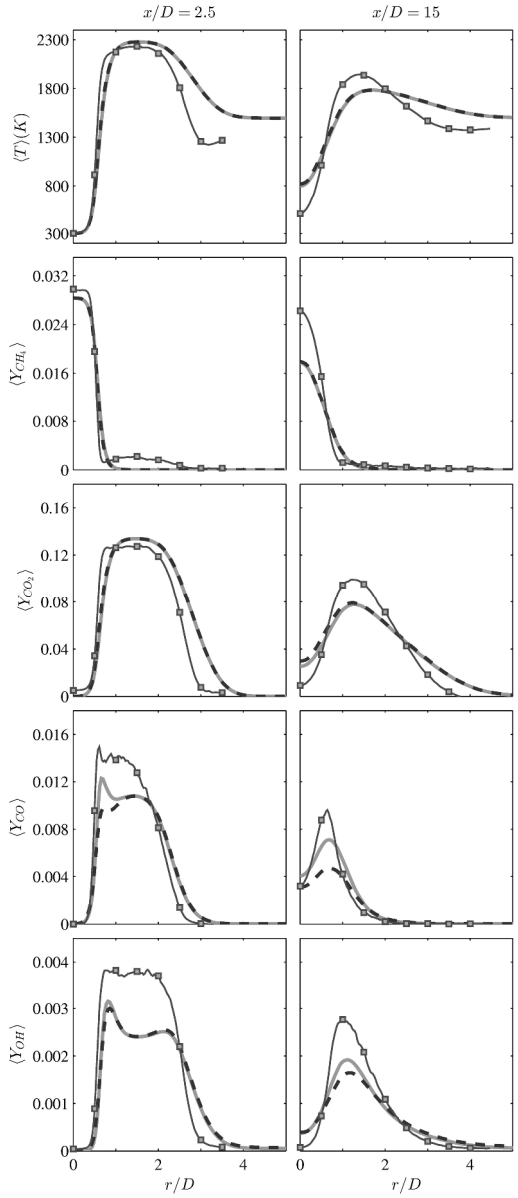

Radial profiles of (from top to bottom) time-averaged mass-weighted mean temperature, and time-averaged mass-weighted mean mass fractions of species CH_4, CO_2, CO, and OH in the RANS-PDF calculations of PM1-50 using different chemistry models and boundary conditions. Left-most two columns: equilibrium boundary conditions and chemistry modeled with: detailed chemistry using ARM-1 and ISAT (dark dashed lines) and FGM-AI (light solid line); Right-most two columns: laminar flame boundary conditions using: ARM-1 and ISAT (light dashed line) and FGM-LF (dark solid line); Lines with squares: experimental data.
264x618mm (300 x 300 DPI)

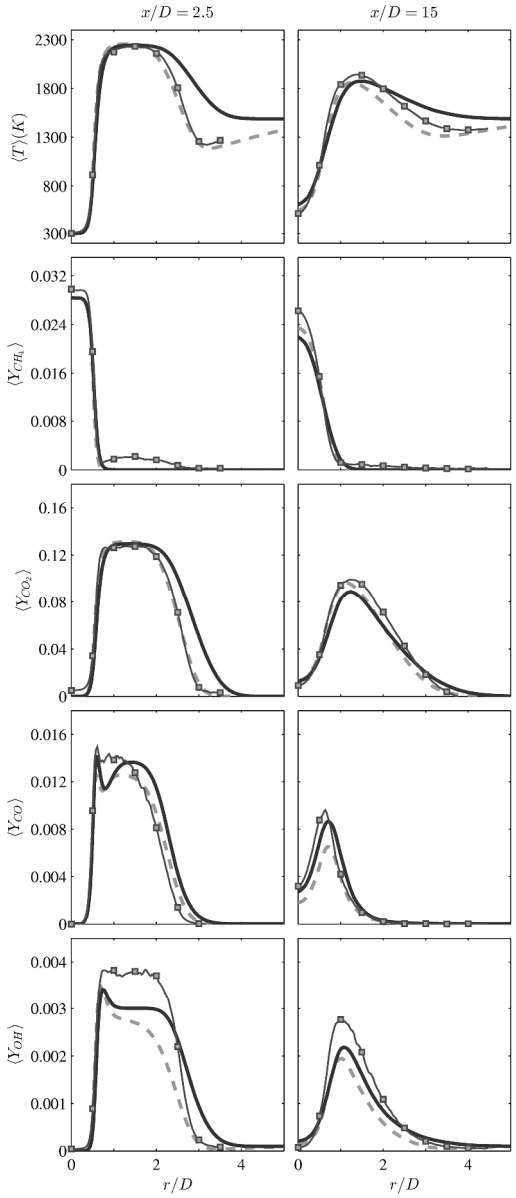

Radial profiles of (from top to bottom) time-averaged mass-weighted mean temperature, and time-averaged mass-weighted mean mass fractions of species *CH₄*, *CO₂*, *CO*, and *OH* in the RANS-PDF calculations of PM1-50 using different chemistry models and boundary conditions. Left-most two columns: equilibrium boundary conditions and chemistry modeled with: detailed chemistry using ARM-1 and ISAT (dark dashed lines) and FGM-AI (light solid line); Right-most two columns: laminar flame boundary conditions using: ARM-1 and ISAT (light dashed line) and FGM-LF (dark solid line); Lines with squares: experimental data.
264x618mm (300 x 300 DPI)

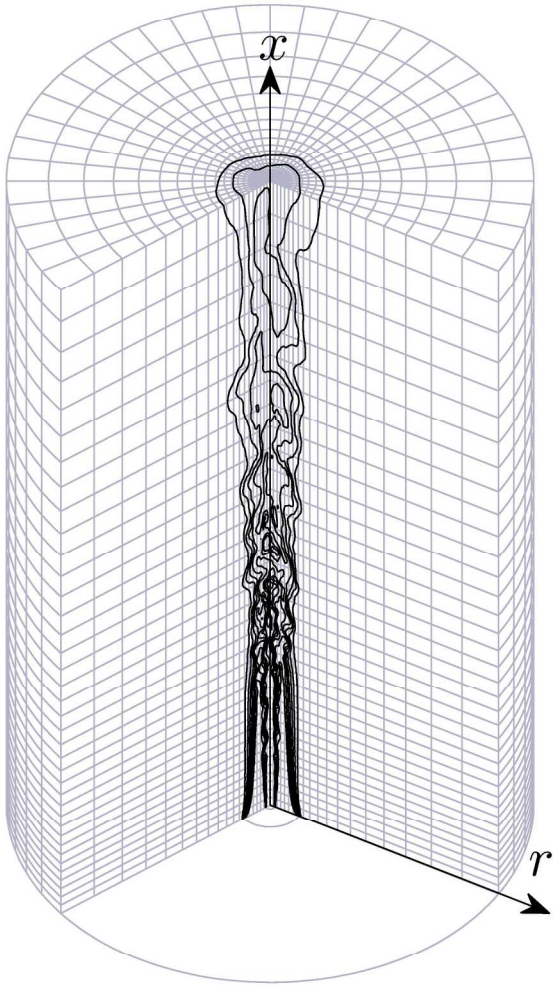

Computational domain for the LES-PDF calculations. The axial and radial directions are indicated by the arrows, and the vertical arrow coincides with the centerline of the jet. Only one fifth of the grid points from grid G3 are shown in each axial and radial direction. The cutaway in the *x*-*r* plane shows a contour of the instantaneous resolved CO_2 mass fraction from a calculation of PM1-100.In the plane at the bottom of the cutaway, the diameter of the pilot and jet are shown.
158x238mm (300 x 300 DPI)

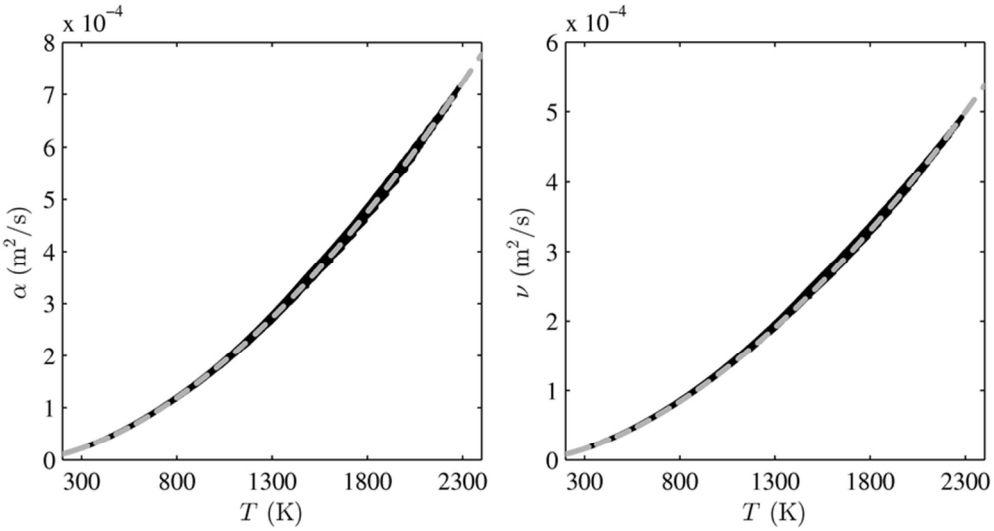

Molecular transport properties as prescribed in LES-PDF calculations as functions of temperature. The thermal diffusivity is shown in the left plot, and the kinematic viscosity is shown in the right plot. In both plots, the black dots indicate the transport properties as evaluated on the FGM, and the gray dashed lines indicate the curve-fits used to Eqs.2 and 7 that are prescribed in the LES-PDF calculations.
77x41mm (300 x 300 DPI)

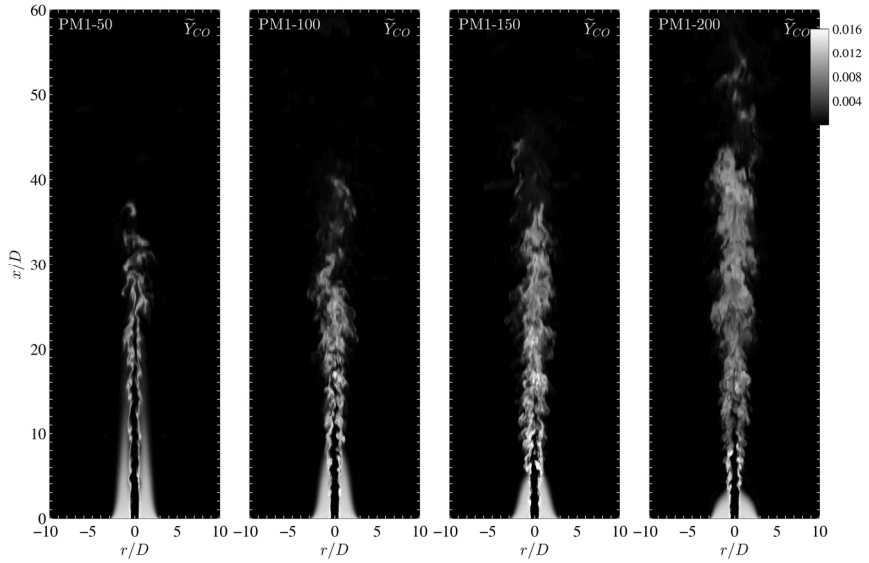

Contour plots of instantaneous fields of resolved *CO* mass fraction from LES-PDF calculations of all four PPJB flames on grid G4 using the mechanism ARM-1 to describe the chemistry.
171x109mm (300 x 300 DPI)

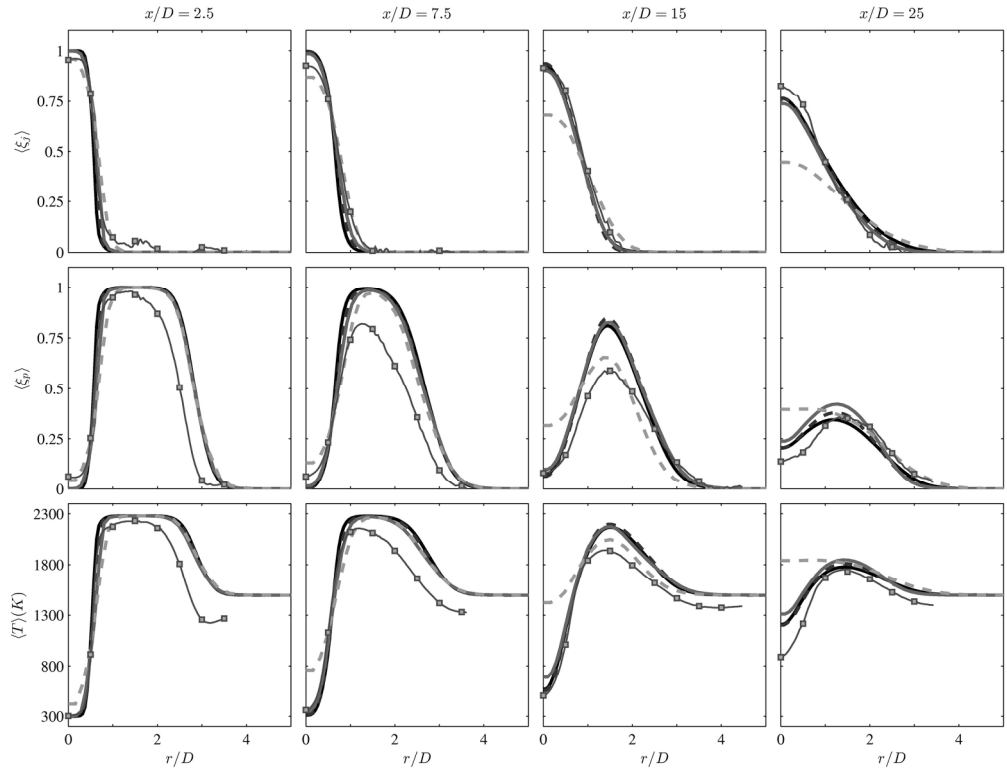

Radial profiles of the time-averaged mass-weighted resolved mean (a) and RMS of the resolved scalar (b) for the jet mixture fraction (top row), pilot mixture fraction (middle row), and temperature (bottom row) in the convergence study of the LES-PDF calculations of flame PM1-50. The axial location is indicated at the top of each column. Dashed light gray: G1; Solid gray: G2; Dashed dark gray: G3; Solid black: G4; Lines with squares: experimental data.
179x138mm (300 x 300 DPI)

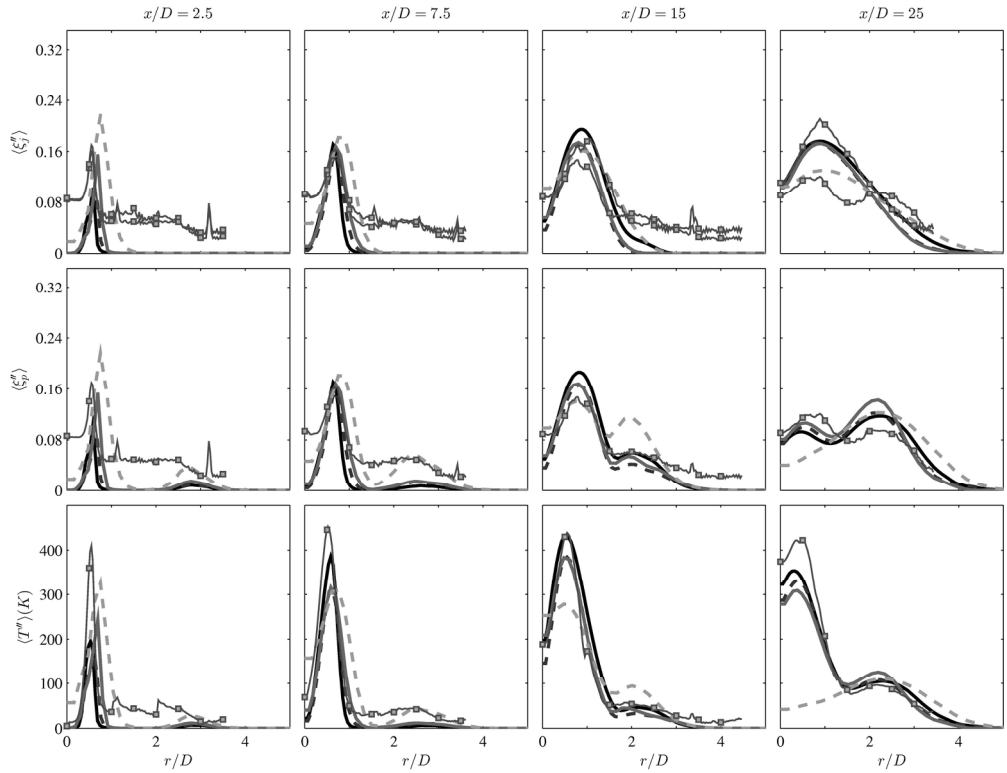

Radial profiles of the time-averaged mass-weighted resolved mean (a) and RMS of the resolved scalar (b) for the jet mixture fraction (top row), pilot mixture fraction (middle row), and temperature (bottom row) in the convergence study of the LES-PDF calculations of flame PM1-50. The axial location is indicated at the top of each column. Dashed light gray: G1; Solid gray: G2; Dashed dark gray: G3; Solid black: G4; Lines with squares: experimental data.
179x138mm (300 x 300 DPI)

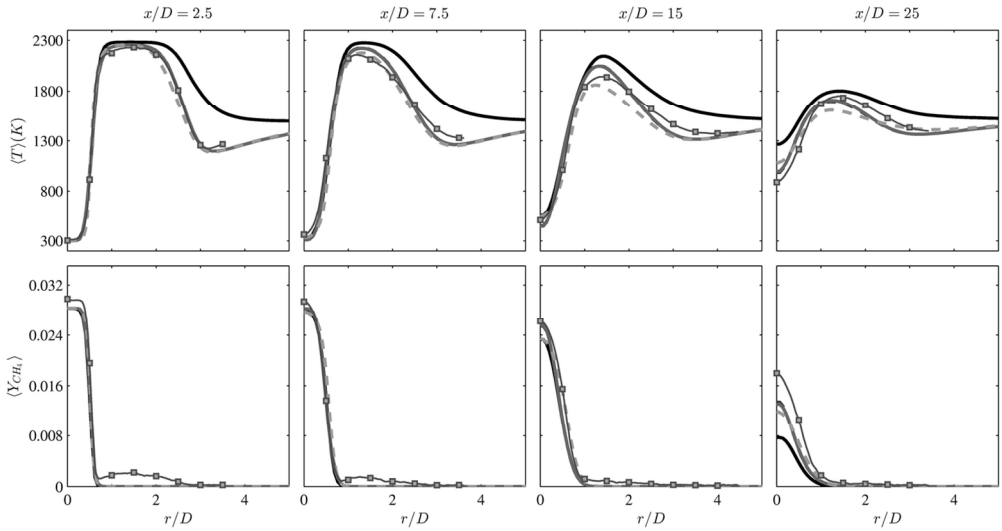

Radial profiles of the time-averaged mass-weighted resolved mean (a) and RMS (b) statistics in the base case LES-PDF and RANS-PDF calculations of flame PM1-50. Dark solid line: LES-PDF without heat loss; Gray solid line: LES-PDF with heat loss (total RMS); Gray dashed line: LES-PDF with heat loss (RMS of resolved scalar); Light gray dashed line: base case RANS-PDF; Lines with squares: experimental data.
124x66mm (300 x 300 DPI)

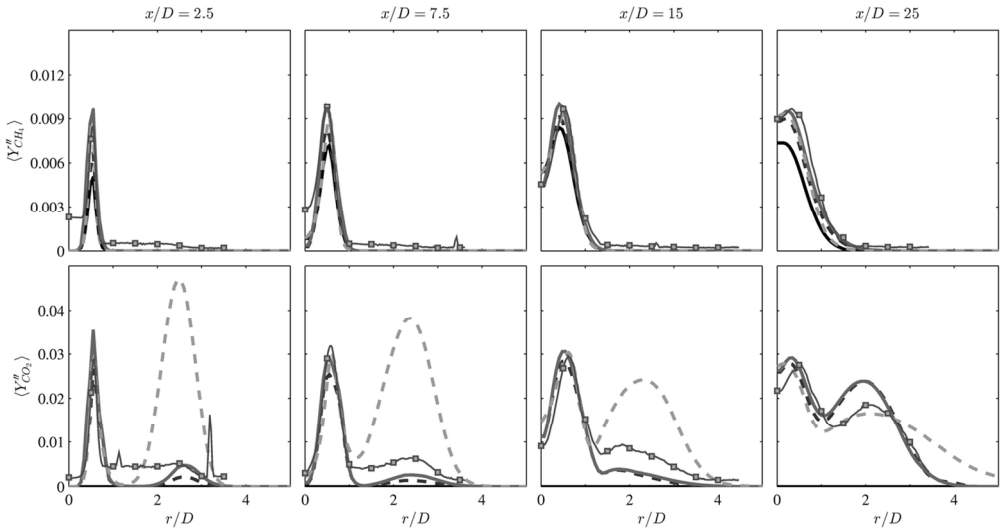

Radial profiles of the time-averaged mass-weighted resolved mean (a) and RMS (b) statistics in the base case LES-PDF and RANS-PDF calculations of flame PM1-50. Dark solid line: LES-PDF without heat loss; Gray solid line: LES-PDF with heat loss (total RMS); Gray dashed line: LES-PDF with heat loss (RMS of resolved scalar); Light gray dashed line: base case RANS-PDF; Lines with squares: experimental data.
124x66mm (300 x 300 DPI)

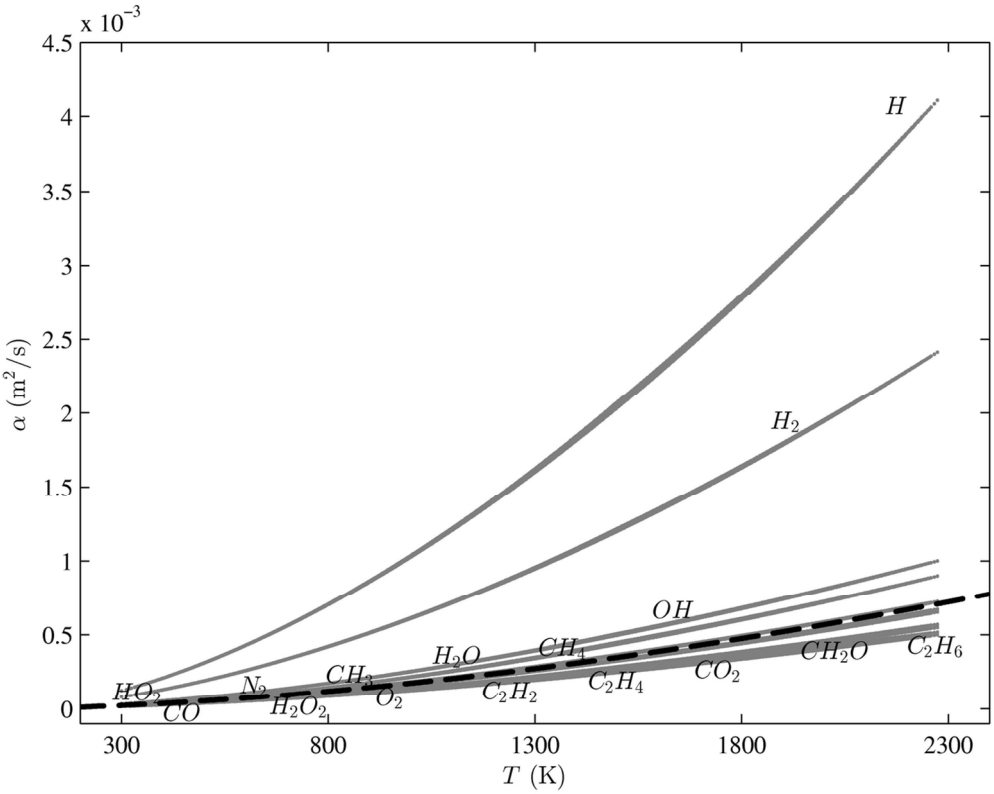

Molecular diffusivity of the chemical species in the ARM-1 mechanism as evaluated from compositions on the FGM and plotted as functions of temperature. The curve-fit to Eq.2 for the thermal diffusivity is shown by the black dotted line.
114x91mm (300 x 300 DPI)

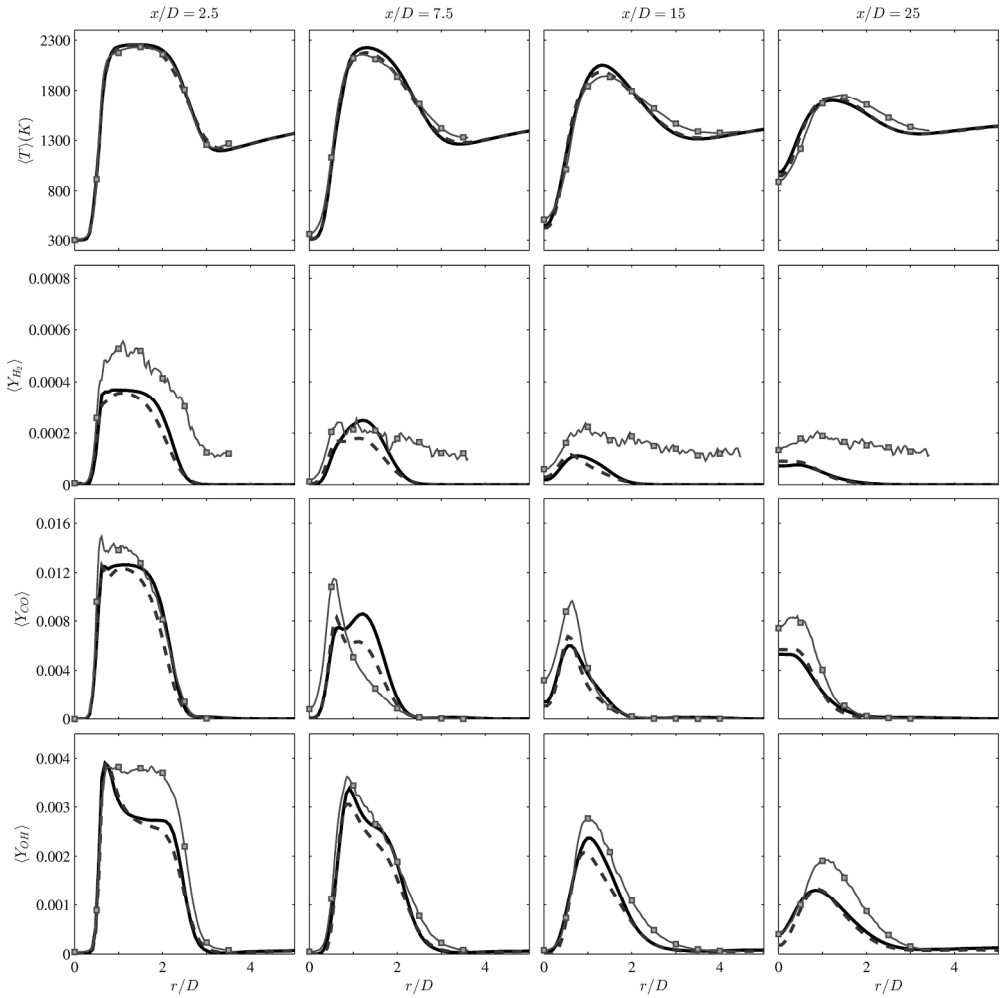

Radial profiles of time-averaged mass-weighted resolved scalars in calculations of PM1-50 with and without differential diffusion. The first row shows the temperature, the next three rows show the mass fraction of the species H_2, *CO*, and *OH*. Solid dark line: Without differential diffusion; Dashed gray line: with differential diffusion; Lines with squares: experimental data.
233x233mm (300 x 300 DPI)

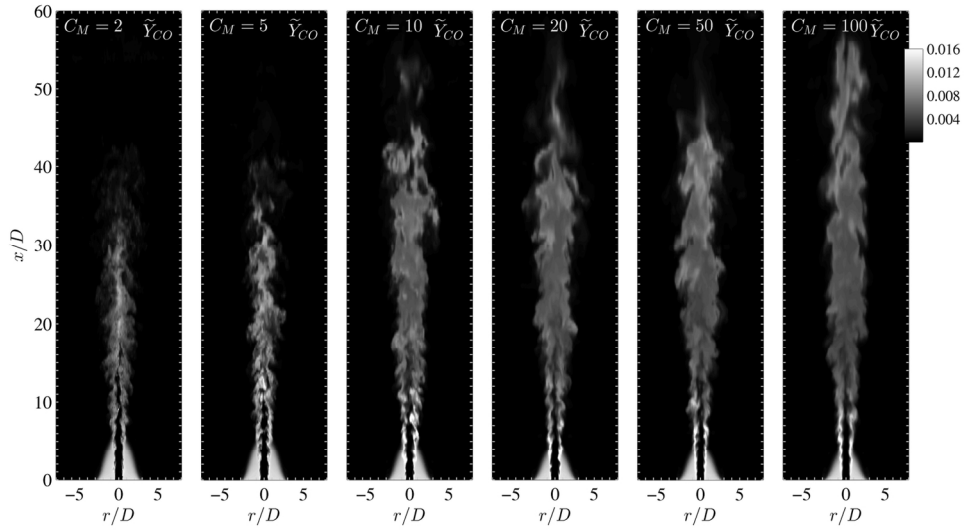

Contour plots of instantaneous resolved mass fraction of *CO* in the parametric study of C_M for flame PM1-150. The value of C_M used in each calculation increases from 2 to 100 going from left to right, and is indicated in the top left corner of each plot. The value of the resolved *CO* mass fraction is indicated by the colorbar in the top right corner.
145x89mm (300 x 300 DPI)

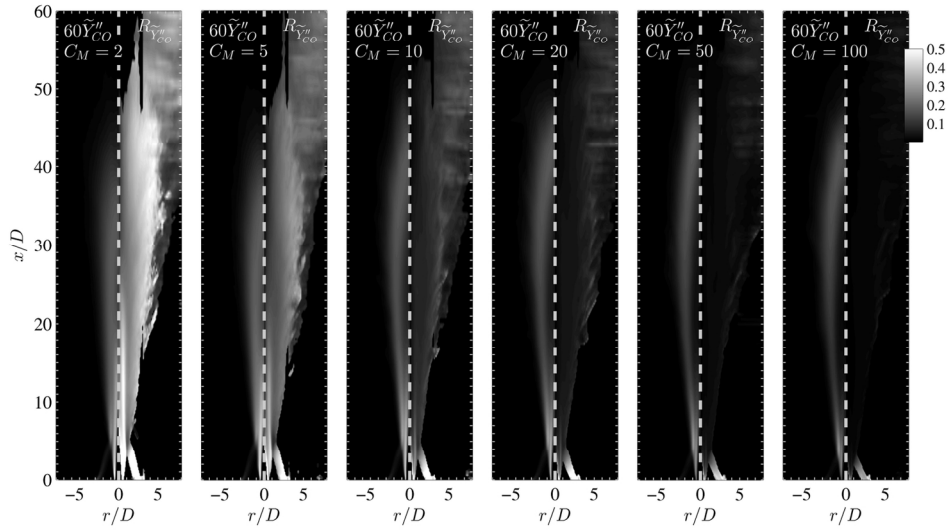

Contour plots of time-averaged mass-weighted total RMS of *CO* mass fraction (left side) and portion of the total RMS which is residual, R_{CO}, (right side) in the parametric study of C_M for flame PM1-150. The quantity R_{CO} is defined as the time-averaged mass-weighted residual RMS mass fraction of *CO* divided by the time-averaged mass-weighted total RMS mass fraction of *CO*. The magnitude of the total RMS (left side) is multiplied by a factor of 60 so one colorbar is used to show the magnitude of both quantities.
145x89mm (300 x 300 DPI)

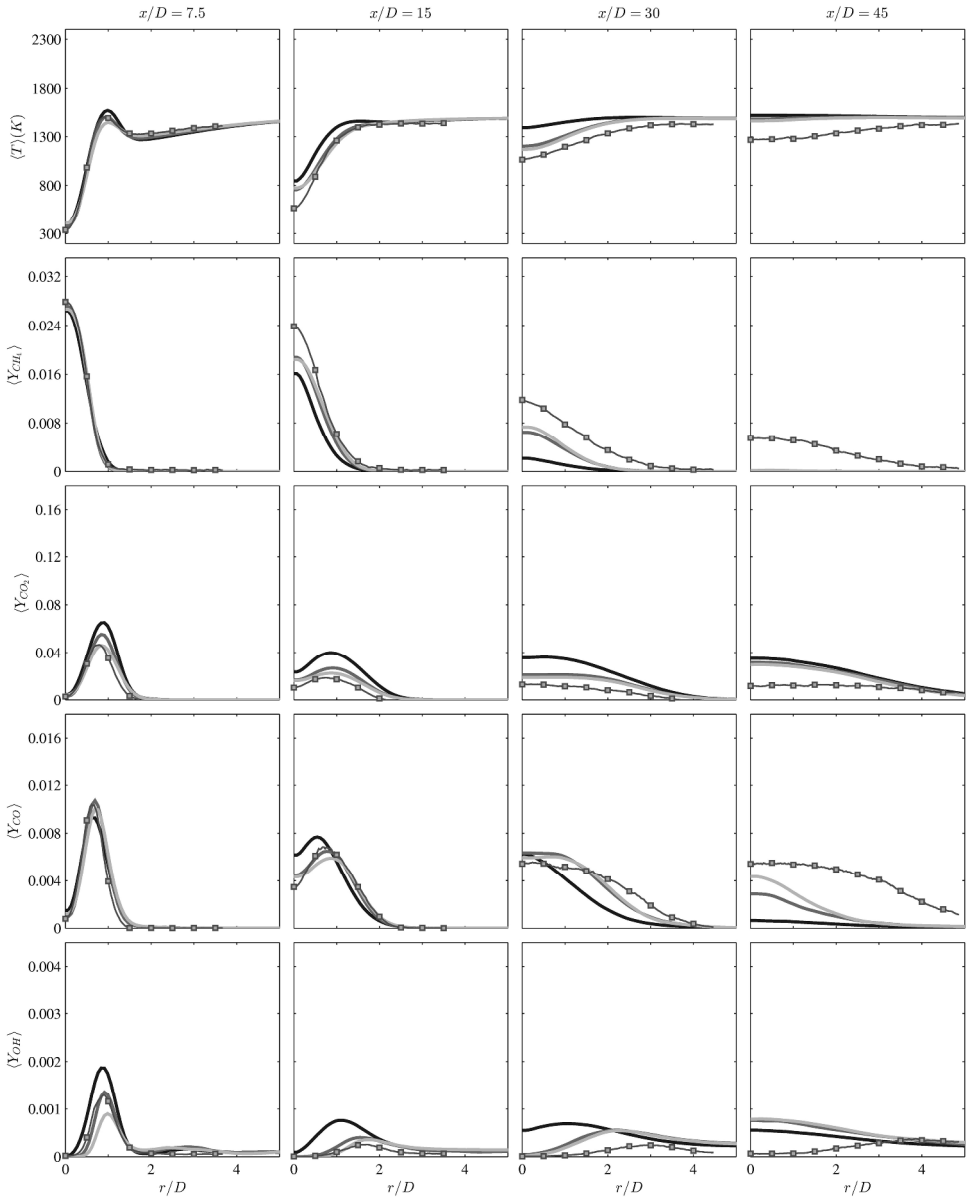

Radial profiles of time-averaged mass-weighted mean of resolved scalars in the parametric study of C_C in flame PM1-150. The plotted scalars are, from top row to bottom row, temperature and mass fractions of the species CH_4, CO_2, CO, and OH. Black line: C_C=5; Dark gray line: C_C=20; Light gray line: C_C=50; Lines with squares: experimental data.
288x358mm (300 x 300 DPI)

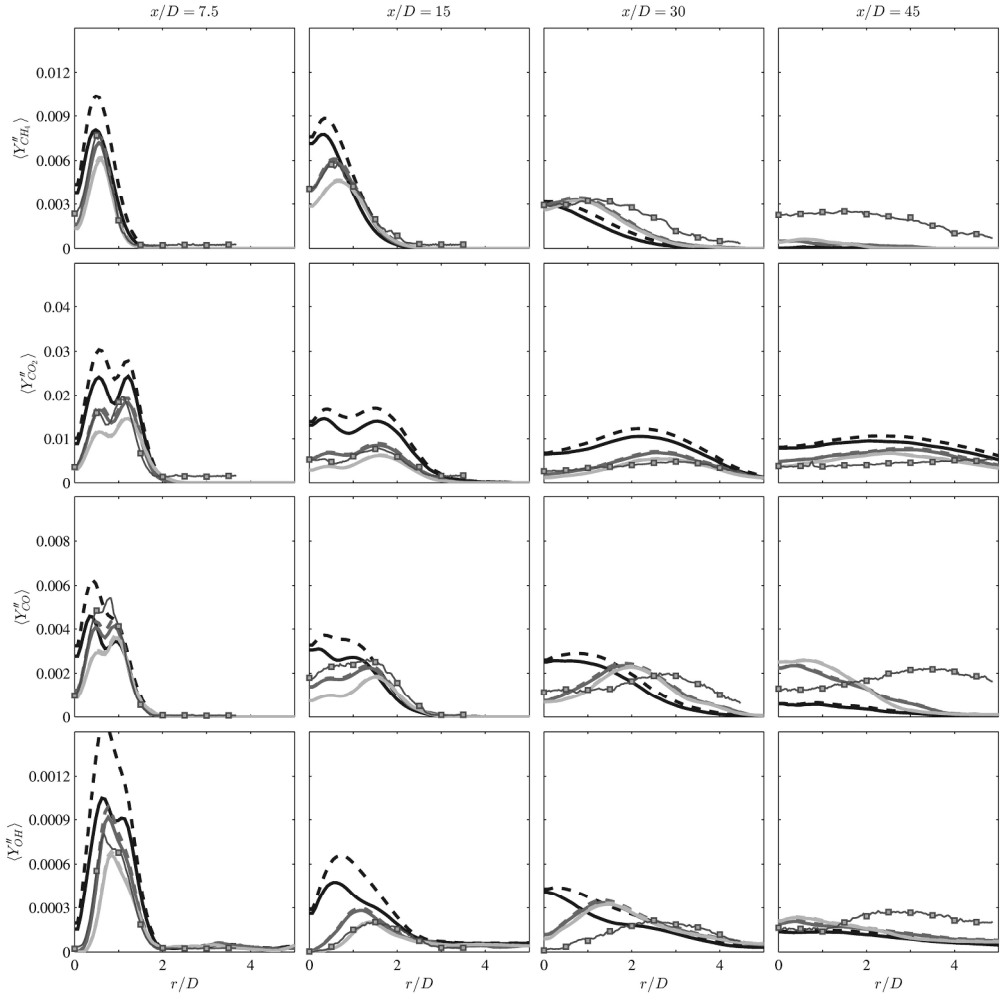

Radial profiles of time-averaged mass-weighted RMS of resolved scalars and total RMS (RMS of resolved fields and residual RMS) in the parametric study of C_C in flame PM1-150. The plotted scalars are, from top row to bottom row, temperature and mass fractions of the species CH_4, CO_2, CO, and OH. Black line: C_C=5; Dark gray line: C_C=20; Light gray line: C_C=50; Lines with squares: experimental data.
233x233mm (300 x 300 DPI)

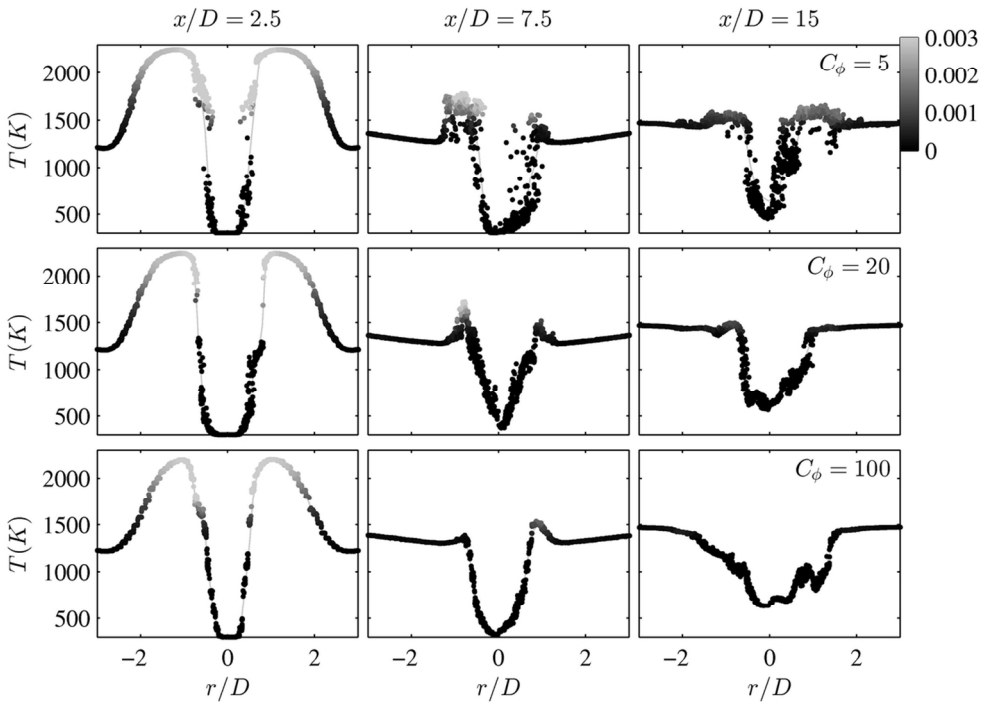

Radial profiles of instantaneous particle quantities from the parametric study of C_M from flame PM1-150. The topmost three rows (a) show the temperature of the particles as a function of the radial position for one row of cells in the calculations. The bottommost three rows (b) show the temperature deviation from the cell mean temperature for the same particles in the same one row of cells. For each set of three columns, the axial location of the plots increase from left to right as indicated above each column. Each row shows results from calculations using a different value of C_M, increase from top row to bottom row as C_M of 5 (top row), C_M of 20 (middle row), and C_M of 100 (bottom row). The particles in the topmost three rows (a) are colored by the particle *CO* mass fraction, and the particles in the bottommost three rows (b) are colored by the deviation of the *CO* mass fraction from the cell mean *CO* mass fraction. The light solid line in the topmost three rows (a) indicates the cell mean temperature for the row of cells plotted.
111x83mm (300 x 300 DPI)

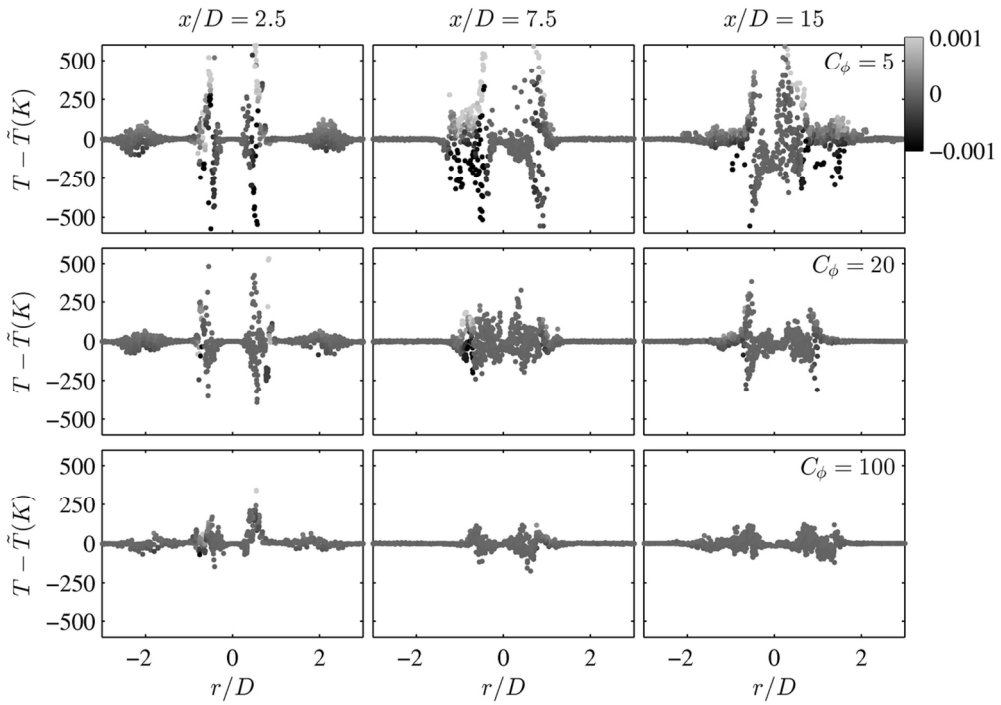

Radial profiles of instantaneous particle quantities from the parametric study of C_M from flame PM1-150. The topmost three rows (a) show the temperature of the particles as a function of the radial position for one row of cells in the calculations. The bottommost three rows (b) show the temperature deviation from the cell mean temperature for the same particles in the same one row of cells. For each set of three columns, the axial location of the plots increase from left to right as indicated above each column. Each row shows results from calculations using a different value of C_M, increase from top row to bottom row as C_M of 5 (top row), C_M of 20 (middle row), and C_M of 100 (bottom row). The particles in the topmost three rows (a) are colored by the particle *CO* mass fraction, and the particles in the bottommost three rows (b) are colored by the deviation of the *CO* mass fraction from the cell mean *CO* mass fraction. The light solid line in the topmost three rows (a) indicates the cell mean temperature for the row of cells plotted.
111x83mm (300 x 300 DPI)

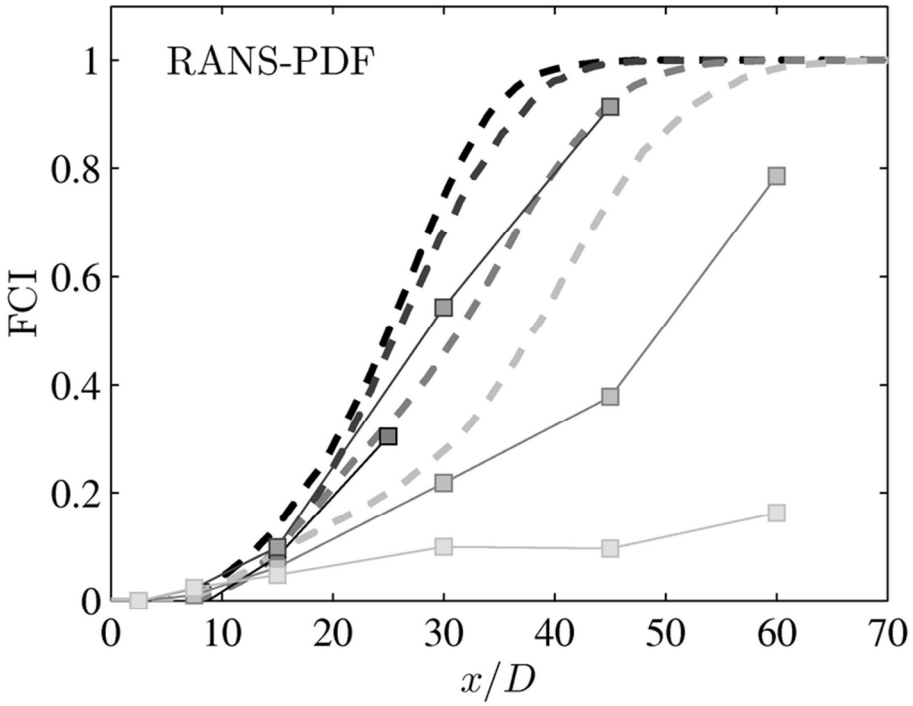

Fuel Consumption Index (FCI) on the centerline of the jet (*r/D=0*) as a function of axial position (*x/D*) from the experimental measurements of the PPJB flames and various calculations from this study. In all plots, the experimental measurements are denoted by the lines with square markers. The leftmost plot (a) shows the results from the RANS-PDF calculations in the dashed lines. The rightmost plot (b) shows the results from the LES-PDF calculations in the solid lines. In both (a) and (b), the color of the line denotes the flame. The darkest line is for PM1-50, the second darkest is for PM1-100, the second lightest is for PM1-150, and the lightest is for PM1-200. In the rightmost plot (c), the results from the parameter study of C_M in the LES-PDF calculations of PM1-150 are shown. The line colors, from dark to light, denote values of C_M of 5, 10, 20, 50, and 100.

79x59mm (300 x 300 DPI)

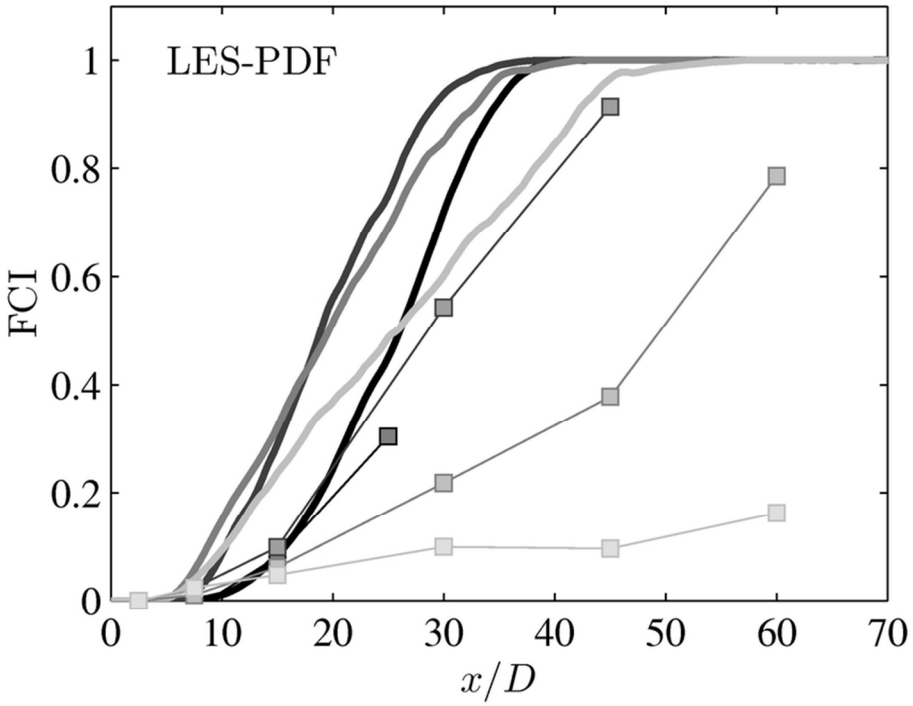

Fuel Consumption Index (FCI) on the centerline of the jet (*r/D=0*) as a function of axial position (*x/D*) from the experimental measurements of the PPJB flames and various calculations from this study. In all plots, the experimental measurements are denoted by the lines with square markers. The leftmost plot (a) shows the results from the RANS-PDF calculations in the dashed lines. The rightmost plot (b) shows the results from the LES-PDF calculations in the solid lines. In both (a) and (b), the color of the line denotes the flame. The darkest line is for PM1-50, the second darkest is for PM1-100, the second lightest is for PM1-150, and the lightest is for PM1-200. In the rightmost plot (c), the results from the parameter study of C_M in the LES-PDF calculations of PM1-150 are shown. The line colors, from dark to light, denote values of C_M of 5, 10, 20, 50, and 100.

79x59mm (300 x 300 DPI)

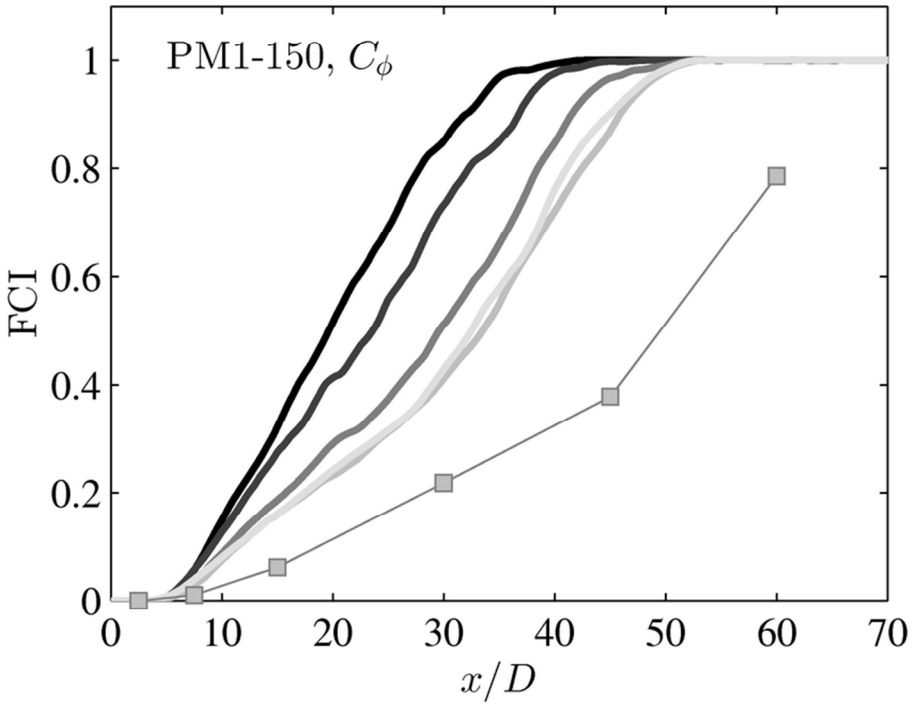

Fuel Consumption Index (FCI) on the centerline of the jet (*r/D=0*) as a function of axial position (*x/D*) from the experimental measurements of the PPJB flames and various calculations from this study. In all plots, the experimental measurements are denoted by the lines with square markers. The leftmost plot (a) shows the results from the RANS-PDF calculations in the dashed lines. The rightmost plot (b) shows the results from the LES-PDF calculations in the solid lines. In both (a) and (b), the color of the line denotes the flame. The darkest line is for PM1-50, the second darkest is for PM1-100, the second lightest is for PM1-150, and the lightest is for PM1-200. In the rightmost plot (c), the results from the parameter study of C_M in the LES-PDF calculations of PM1-150 are shown. The line colors, from dark to light, denote values of C_M of 5, 10, 20, 50, and 100.

79x59mm (300 x 300 DPI)